FIBER SHAPE EFFECTS ON THE COMPRESSIVE STRENGTH OF

UNIDIRECTIONAL CARBON FIBER COMPOSITES: A COMPUTATIONAL STUDY

by

Ryan Clarke

A thesis submitted in partial fulfillment
of the requirements for the degree

of

Master of Science

in

Mechanical Engineering

MONTANA STATE UNIVERSITY
Bozeman, Montana

April 2020

ACKNOWLEDGEMENTS

TABLE OF CONTENTS

TABLE OF CONTENTS – CONTINUED

v

LIST OF TABLES

LIST OF FIGURES – CONTINUED

LIST OF FIGURES – CONTINUED

LIST OF FIGURES – CONTINUED

ABSTRACT

The tensile strength tends to be much higher than the compressive strength for carbon fiber reinforced polymer composites because of a change in failure modes. Current research activities are looking at novel precursors for reducing overall costs of carbon fiber production. The potential cost savings in new precursor carbon fiber make it economically feasible to use in large structural components. Some fiber precursors and manufacturing methods produce carbon fibers that have a kidney-shaped cross-section whereas traditional carbon fiber is circular. The aim of this study is to investigate the differences in compressive failure responses between fiber shapes in carbon fiber composites. A finite element micromechanical model was developed in ABAQUS of a single carbon fiber embedded in a square matrix with periodic boundary conditions. Two fiber cross-sectional geometries were examined: circular and kidney shaped. Three factors that affect the compressive failure response of carbon fiber reinforced polymers were investigated. These include fiber misalignment, volume fraction, and multiaxial loading.

The results showed negligible differences between the compressive failure response of fibers with different cross-sectional shapes. Compressive strength was shown to have a decaying sensitivity to increasing fiber misalignment. Decreasing the volume fraction did decrease the compressive strength but also increased the compressive failure strain. In addition, adding in-plane shear loads proved detrimental to the compressive load-carrying capacity of a composite structure. This research showed minimizing fiber misalignment in manufacturing processes is only beneficial for high tolerance processes. In addition, decreasing volume fraction could be beneficial for highly flexible structures. Finally, the results demonstrated the need to minimize multiaxial loading for optimal composite compressive response.

INTRODUCTION

Motivation

Energy production is a rapidly changing market in modern society. While the past two centuries have seen remarkable growth and modernization with fossil fuels as its main energy source; today's energy needs, and the non-renewable nature of fossil fuels has driven the energy market towards renewable, "greener" sources of energy. Wind energy is one of the largest renewable energy generation types, making up more than 1/3 of all utility-scale renewable energy generation in the U.S in 2019. Wind energy has also shown remarkable growth in the past 10 years at the utility scale, having increased 270% since 2009 [1].

One reason for the impressive growth in utility scale wind power over the last decade is the increase in rotor diameter of the turbines themselves. Larger turbines mean that less are needed for the same energy production therefore reducing operations cost. This trend in increasing turbine size is expected to continue for the foreseeable future (Figure 1) to maintain wind energy's cost competitiveness and keep up with global energy demand.
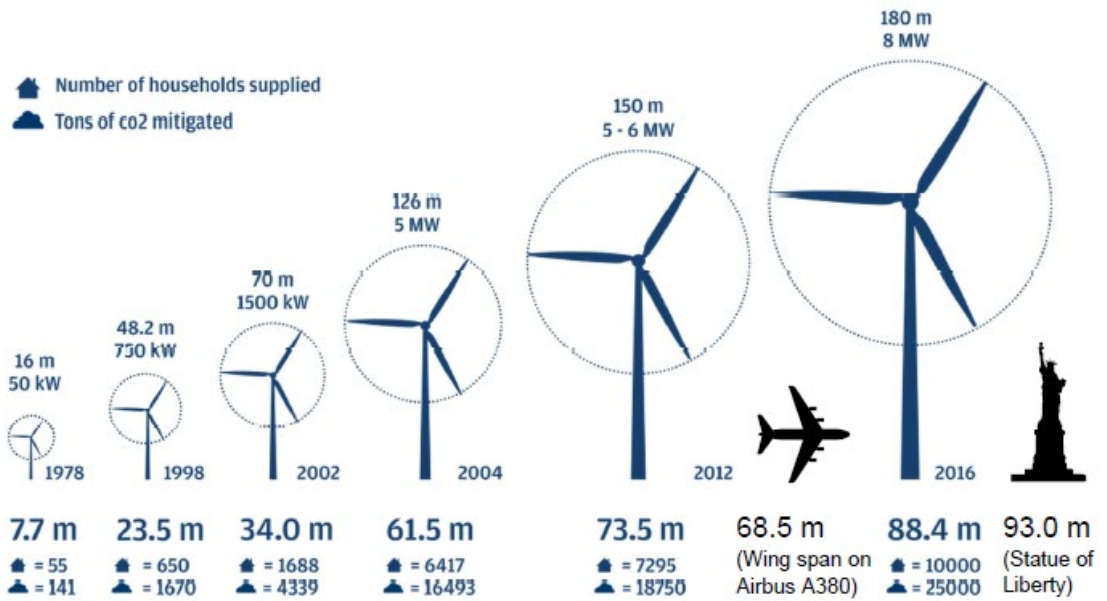
Figure 1: Evolution of wind turbine size over the years [2]

As wind turbines continue to grow in size, the weight of the rotor continues to grow at an ever-increasing rate illustrated in Figure 2. With increasing size and weight of wind blades the structural performance requirements become more difficult to achieve.
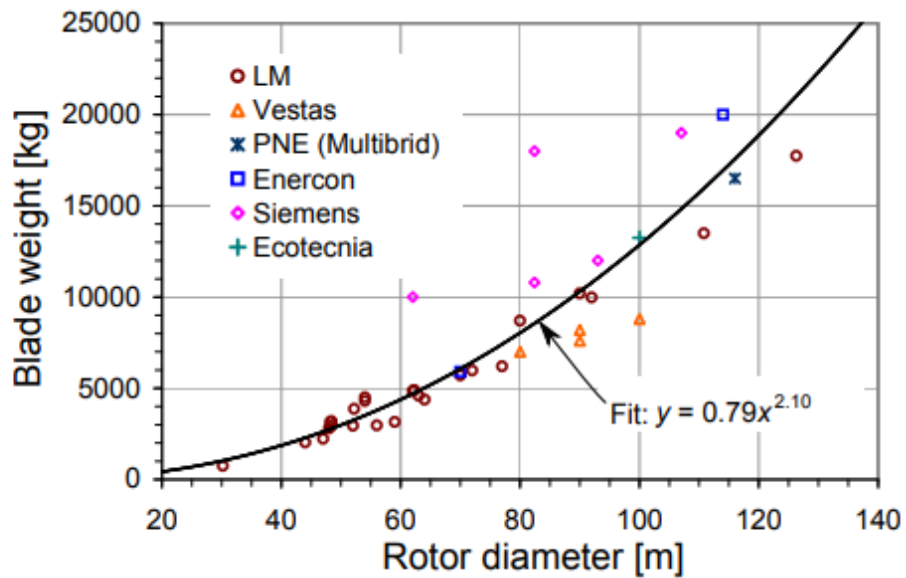
Figure 2: Trend in blade mass with increasing rotor diameter [3]

To maintain acceptable levels of structural performance needed for a service lifetime of at least 20 years or more, either the structural geometry (Figure 3) or the materials of the wind turbine rotor can be modified. One solution to this problem is to replace the traditional materials, Glass Fiber-Reinforced Polymer Composites (GFRP), that structural wind turbine spar caps are made from with stronger, stiffer materials, such as Carbon Fiber Reinforced Composites (CFRP).
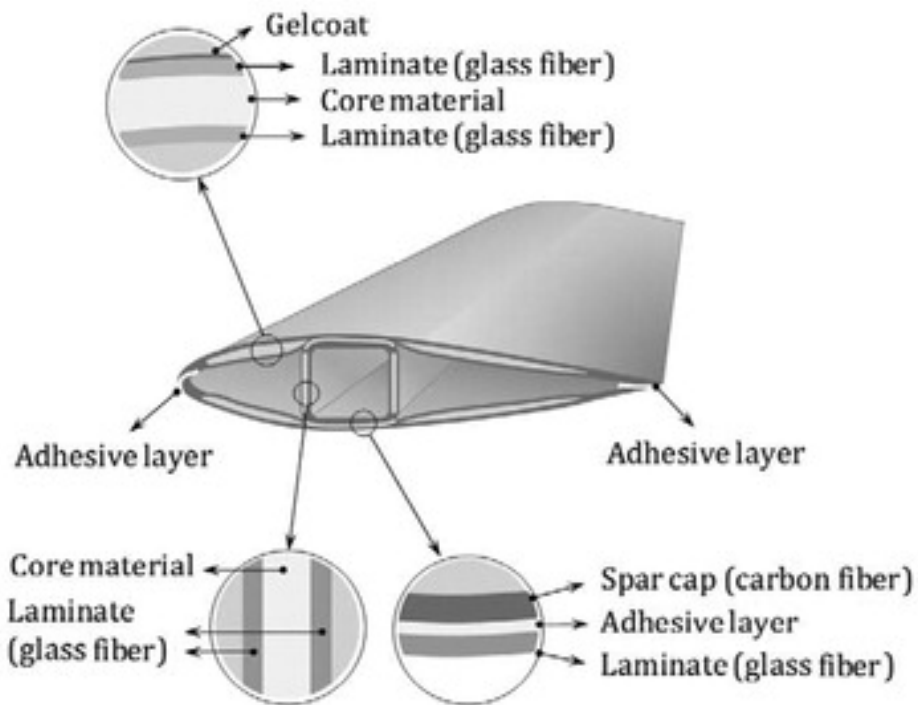
Figure 3: Cross-section view of a typical wind turbine blade [4]

Historically, CFRP have been too expensive to be considered for widespread use in wind turbine blades. However, recent research into novel precursors for carbon fiber production has dramatically reduced the overall cost of CFRP materials. CFRP material cost reduction coupled with a low cost, high volume manufacturing method such as pultrusion has made CFRP an economically viable material for use in large scale structures

[4]. An interesting characteristic of this novel low cost carbon fiber is it can be produced with a kidney-shaped cross section (Figure 4), as opposed to the traditional circular cross section seen in most commercial carbon fiber. This change in fiber shape has the potential to change the mechanical response of the composite.
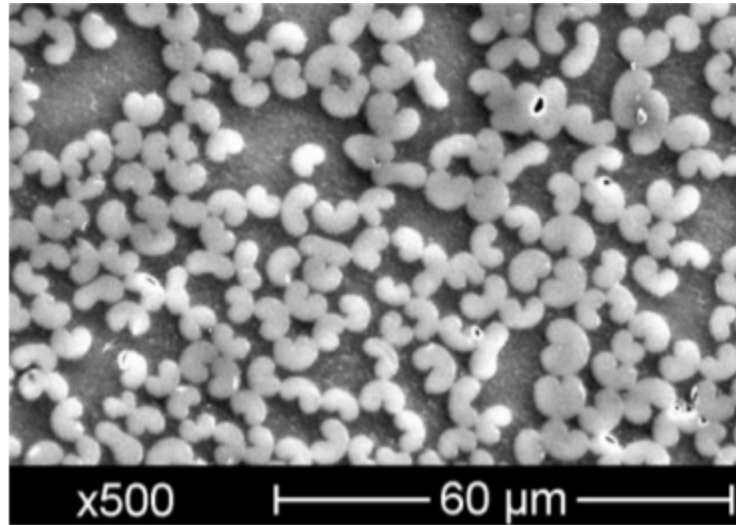
Figure 4: Micrograph of kidney shaped carbon fiber [4]

A limiting design factor in all structures made from Fiber-Reinforced Composites is the relatively low compressive strength capabilities of these materials compared to their tensile strength. There seems to be a disconnect between composite manufactures and wind turbine designers in this area. Composite manufactures continue to optimize for what composites are inherently good at, tensile strength. Whereas wind turbine designers are limited by the low compressive strength of the materials they are using and cannot take full advantage of the material's tensile properties.

<u>Objectives</u>

To be able to build larger, more durable wind blades a better understanding of the factors affecting the compressive strength of CFRP materials needs to be achieved. The overall objective of this thesis is to:

1. Investigate the effect that the kidney-shape geometry has on the compressive strength of CFRP materials.

There are four secondary objectives that can in part give a deeper understanding of the primary objective but can also be standalone result. The four secondary objectives are as follows:

2. Investigate the validity of a 3-D micromechanical model to predict CFRP compressive failure.

3. Examine the effect of fiber angle defect severity has on CFRP compressive failure.

4. Examine the effect volume fraction has on CFRP compressive failure.

5. Examine the effect varying degrees of multiaxial loading have on CFRP compressive failure.

An important clarification is that the objective of this thesis is not to develop a model that can accurately predict the compressive strength of a CFRP composite. Instead, this is a comparative study of different factors that affect compressive strength. The models developed herein accurately capture the overall physics of the problem while maintaining computational efficiency.

Methods

To complete the five objectives for this research a composite micromechanics model was developed using the Finite Element Method (FEM) to discretely analyze local effects like fiber cross-sectional shape have on the compressive failure response of the composite structure as a whole.

FEM is a numerical analysis method where a structure is discretized or meshed into smaller sub volumes called elements. The elements are connected to one another via nodes at their boundaries. This mesh is used to solve differential equations that describe a field variable within the structure such as displacement. This differential equation is solved piecewise with the elements by approximating the differential equation as a series of algebraic functions. The algebraic equations solved give an approximation of the field solution. Generally speaking, when more elements are used to approximate a structure and the mesh is refined the closer the approximate solution becomes to the exact solution. A more complete explanation of how FEM works is included in Cook et al [5]. The specific analyses within FEM that were used will be described in more detail in the Theory section of this thesis.

THEORY

A thorough literature review has been conducted to first explain the foundational background information needed to fully understand the problem outlined in the previous chapter. Second, explore similar work that has been done previously on the subject being studied. Finally, explain the computational methods that were used to conduct the study in this thesis and their associated implications.

Composite Materials

A composite material is defined as a combination of two or more distinct materials to form a new material with optimized properties [6]. Composites have been used for millennia in various forms; buildings constructed in Mesopotamia over 4000 years ago have been found constructed from mud reinforced with straw. The Mongols used a composite bow taking advantage of the elastic properties of tendon and the compressive properties of bone. In the modern era, all engineered materials can be put into three categories: metals, ceramics, and polymers. Metals offer high toughness, strength and durability, ceramics are extremely hard and stiff with good corrosion-resistant properties, polymers have low density and low cost. Composites when used correctly exploit the various benefits of these materials while mitigating their drawbacks.

Composite materials are often classified by their reinforcement. The three most common reinforcements include: particles, flakes, and fibers as seen in Figure 5. The focus of this thesis is will be on Fiber-Reinforced Polymer (FRP) Composites.
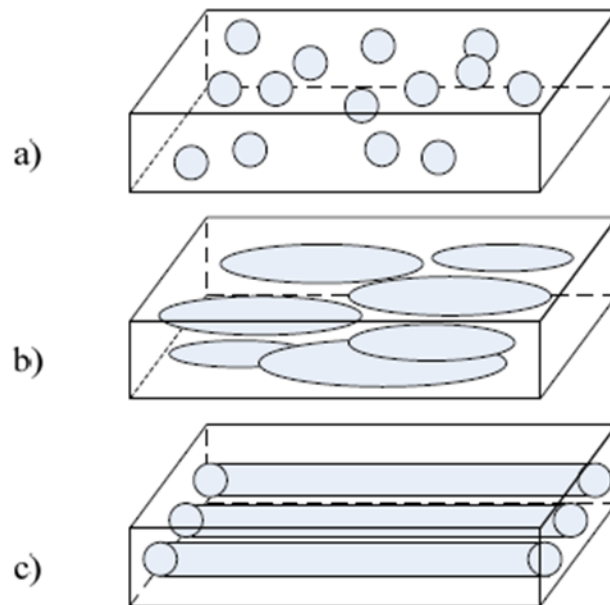
Figure 5: Three types of composite reinforcement: a) particles b) flakes c) fibers. [7]

Fiber-Reinforced Polymer Composites

FRP composites are the main type of composite used in the wind blade industry today because of their high specific strength and specific stiffness; specific means the mass normalized property [8]. The reason that FRP composites can achieve these desirable properties is because of their ability to be engineered to each unique loading cases, by orienting the fibers in the direction of the main loading of that specific structure. FRP composites are advantageous since they can be engineered to maximize strength and stiffness in a specific direction while maintaining a low weight.

The fibers that are mainly used in the wind blade industry are made of glass or carbon that is made as tows. Tows are bundles of straight single fibers that are stitched together into fabric for ease of manufacturing. Unidirectional (UD) fabrics are made from tows that are stitched in parallel to one another, so all the fibers are oriented in the same direction. Biaxial fabrics have tows that are stitched into two main directions usually so

that the two directions are orthogonal to one another. In typical wind blade construction (see Figure 3), biaxial fabric is used in the shell and shear web to resist shearing loads and impact. UD fibers oriented along the major axis of the rotor are used in the spar caps to resist tension and compression caused by the rotor bending. UD carbon fiber reinforcement in the spar cap will be the focus of this thesis.

The polymer matrix material in FRP composites can vary much more than the choice of fiber materials used. Polymers used in FRP composites are classified into two categories thermoset and thermoplastics. Thermosets are more often used in the wind industry because of their lower working viscosity and lower working temperatures. The most popular thermosets used are polyester, vinyl ester, and epoxy. Epoxy is the most widely used thermoset in the industry because of its superior mechanical properties, consequently, it is also the most expensive of the three named here. Thermoplastics historically have not been used in the wind industry because they are more difficult to work with. However recent research has looked into their use because of the potential benefits they have to offer such as high toughness and recyclability [9].

Micromechanics of Composite Materials

Composite materials are heterogeneous and anisotropic while most other modern materials such as metals and ceramics can be considered homogenous. The heterogeneity inherent in composites allows engineers more flexibility to design the material concurrently with the structure [6]. The drawback of composites is that their global properties are determined by the complex interaction between the fiber and matrix. This complex

interaction makes analysis and characterization more difficult than an isotropic, homogenous material.

While the anisotropy of composites can be handled with a coordinate transformation of the material properties from the material coordinate system to global system or vice versa, the heterogeneity of composite materials is harder to account for. To truly represent a composite structure, a Direct Numerical Simulation (DNS) approach can be used to model a full composite structure that capture each discrete phase. Consequently, the finite element mesh must be small enough to capture the diameter of the fiber, which is usually a few microns. This requires that even a simulation of 1 mm^3 block of CFRP material has the potential to have tens of millions of Degrees of Freedom (DOF), let alone an analysis of a full-scale structure with a DNS approach [10]. While being able to realistically represent a composite structure, DNS has been shown to be prohibitively computationally expensive. A more cost-effective approach is to use micromechanics.

Micromechanics is based on the assumption that a certain "microscopic picture" or representative microstructure of the medium being analyzed can be used in conjunction with appropriate mathematical models to predict the macro-reaction [11]. Using micromechanical models and theory, homogenized effective composite material properties can be extracted to use in design and engineering. Micromechanics is usually the first step in composite design as shown in Figure 6.
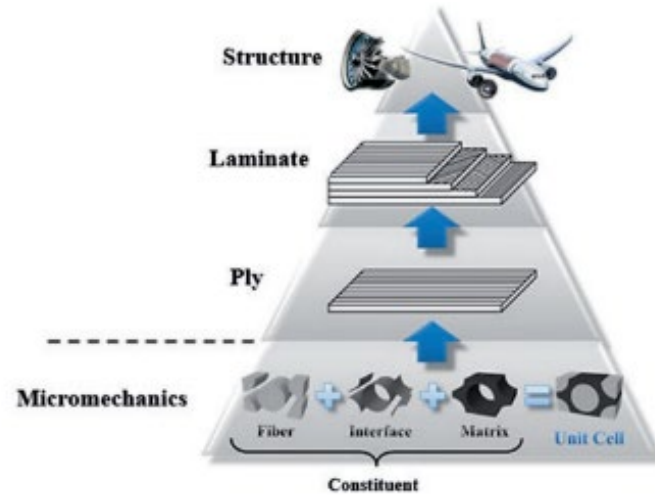
Figure 6: The hierarchy of computational multiscale homogenization modeling [12].

Homogenization Theory and Microstructural Representation

The first step in a micromechanical analysis is to choose an appropriate microstructure. The correct microstructure is not only dependent on the material being analyzed but also the method being used. For example, the simplest micromechanics model is the Rule of Mixtures (ROM) which uses a weighted volume average of the material properties of the constituent materials to obtain effective composite properties. The microstructure for ROM can be described using only the volume fractions of the constituent materials [6]. Volume fraction is defined below in Equation (1):

$$V_f = \frac{Volume\ of\ the\ fibers}{Total\ Volume\ of\ the\ Composite} \tag{1}$$

This work focuses on a numerical micromechanics homogenization scheme known as multiscale computational homogenization, otherwise known as global-local analysis. In multiscale computational homogenization a relationship is developed between macroscopic stress-strain and the microscopic stress-strain in a representative element using specialized boundary conditions and theorems. All microstructural representations in

multiscale computational homogenization can be divided into two main categories, a Representative Volume Element (RVE) and a Repeating Unit Cell (RUC). RVE and RUC are often used interchangeably in the literature but there are a few key differences between these two terms.

An RVE is a volume of a material that is statistically representative of the material as a whole [13]. This definition of an RVE leaves a lot to interpretation. On the one hand, the RVE must be large enough to sufficiently represent the effective homogenized properties independent of the boundary conditions. On the other hand, an RVE must also be small enough to be computationally efficient and justifiable as being a microscopic point in the continuum of the material.

An RUC is an idealization of the bulk material as a periodic array of inclusions. For FRP composites, an RUC is an idealization of fibers embedded in the matrix material. An RUC is much smaller than an RVE and more simplistic. The difference between an RVE and an RUC can be seen in Figure 7.
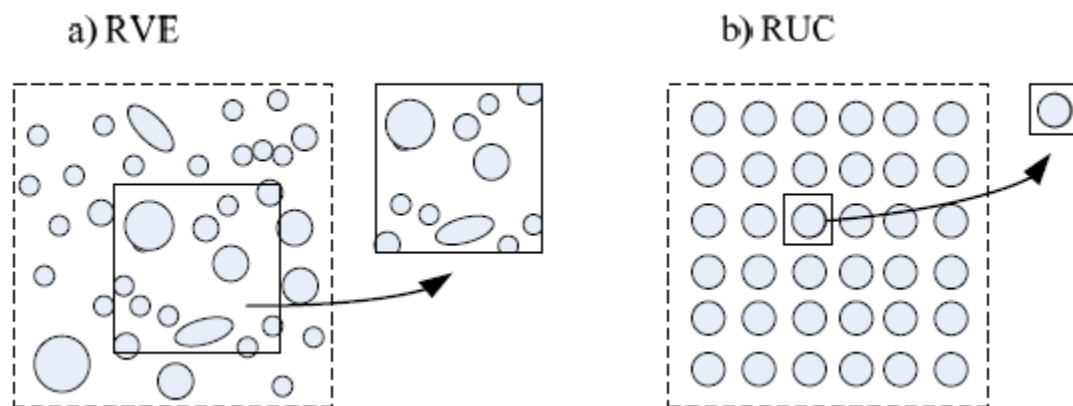
Figure 7: a.) Graphical representation of an RVE b.) Graphical representation of an RUC [7]

Even though an RUC is simpler than an RVE there are still an infinite number of choices for an RUC given a single periodic array as can be seen below in Figure 8.
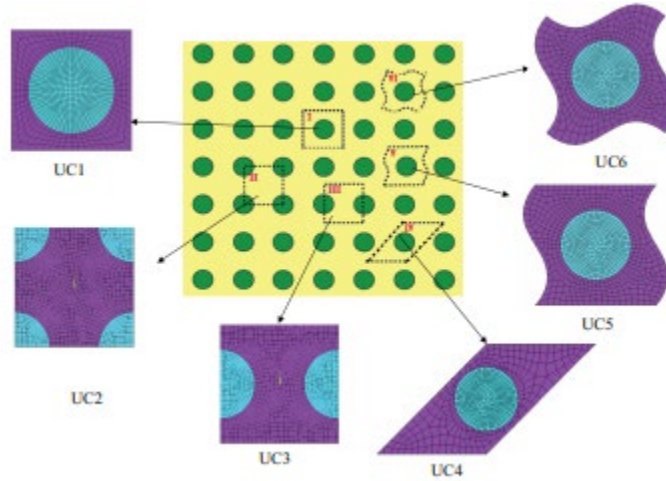
Figure 8: Six different geometry choices for an RUC in a FRP composite [10].

Regardless of whether an RVE or RUC analysis is chosen a fundamental assumption in micromechanics is that on some level the heterogeneities of a material are periodic. The difference between an RVE and an RUC is more a question of the size of the periodicity of the structure. Drago and Pindera (2007) offer a more in-depth discussion of the differences between an RVE and an RUC if the reader is interested [14].

Boundary Conditions

For a micromechanics analysis to be valid the Hill-Mandel Macrohomogeneity Condition must be satisfied [10], [15]. The Hill-Mandel Macrohomogeneity Condition states that the volume-averaged microscopic strain energy density is equivalent to the homogeneous body strain energy density. As shown in Equation (2).

$$U = \frac{1}{2}\bar{\sigma}_{ij}\bar{\varepsilon}_{ij} = \frac{1}{2}\langle\sigma_{ij}\varepsilon_{ij}\rangle \tag{2}$$

The variables $\bar{\sigma}_{ij}$ and $\bar{\varepsilon}_{ij}$ are the macroscopic stress and strain respectively. The term $\langle \sigma_{ij}\varepsilon_{ij} \rangle$ is the volume-averaged microscopic strain energy density field and can also be expressed in integral form as:

$$\langle \sigma_{ij}\varepsilon_{ij} \rangle = \frac{1}{V} \int_V \sigma_{ij}\bar{\varepsilon}_{ij} \, dV = \frac{1}{V} \int_V \bar{\sigma}_{ij}\varepsilon_{ij} dV \tag{3}$$

In the first integral, a microscopic stress field is induced via the introduction of a macroscopic strain. In the second integral, a microscopic strain field is induced via the introduction of macroscopic stress. Macroscopic stress and strain are introduced into a micromechanical analysis as boundary conditions. In an RVE or RUC micromechanical analysis there are three commonly used boundary conditions that satisfy the Hill-Mandel Macrohomogeneity Condition, homogeneous displacement boundary conditions, homogeneous traction boundary conditions, and periodic boundary conditions [10], [16]–[18].

Homogeneous displacement boundary conditions are also known as kinematically uniform boundary conditions. Homogeneous displacement boundary conditions are given in Equation (4).

$$u_i^0 = \bar{\varepsilon}_{ij}y_j \tag{4}$$

The variable u_i^0 is a prescribed displacement at the boundary and y_j are the components of a position vector of a point on the boundary.

The next boundary condition that satisfies the Hill-Mandel Macrohomogeneity Condition is the homogeneous traction boundary conditions given in Equation (5).

$$t_i^0 = \bar{\sigma}_{ij} n_j \tag{5}$$

The variable t_i^0 is the applied surface traction, and n_j is the outward normal of the microstructure boundary being analyzed. The two boundary conditions above are called homogeneous boundary conditions because when they are applied to a homogeneous body, they will produce homogeneous strain and stress field respectively.

The final boundary condition that is commonly used in micromechanical analyses to satisfy the Hill-Mandel Macrohomogeneity condition is Periodic Boundary Conditions (PBCs). PBCs are applied to a micromechanical analysis by ensuring that the displacements and tractions of opposing boundaries of the unit cell are related by Equations (6) and (7).

$$u_i = u_{i'} + \bar{\varepsilon}_{ij} y_j \tag{6}$$

$$T_i = T_{i'} \tag{7}$$

Where u is the displacement T is surface traction and i and i' denote opposing faces of the microstructure being analyzed. PBCs ensure that the surface tractions on opposing faces of a microstructure are equal and opposite to one another while simultaneously ensuring that the displacements of those opposing faces are related with a macroscopic strain term and can be seen as a physical representation below in Figure 9. The traction portion of PBCs is automatically satisfied by the displacement condition in a displacement-based variational method i.e. most finite element solvers. Therefore, in most cases only the displacement portion of the PBCs must be implemented.
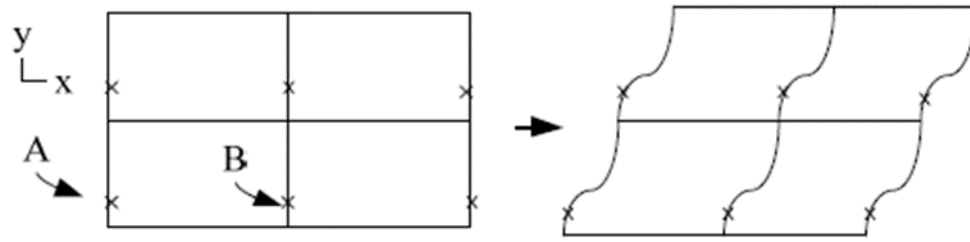
Figure 9: Physical Representation of PBCs [7].

It has been shown in literature that PBCs are the most accurate for prediction of the true effective properties of a heterogeneous material [19]. Homogeneous displacement boundary conditions and homogeneous traction boundary conditions provide an upper and lower limit that converges to periodic with increasing RVE size as shown in Figure 10. Historically, PBCs have not been used in most micromechanical FEA analyses until relatively recently because of the difficulty involved in their implementation. With many commercial FEA packages including coupled constraint equations into their capabilities it has become much more reasonable to implement PBCs.
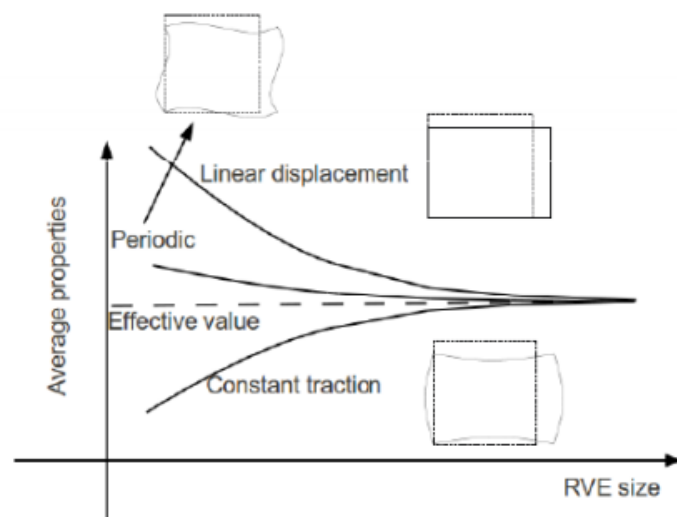
Figure 10: Convergence of different boundary conditions showing their respective physical representation in microscale modeling

Compressive Failure of Fiber-Reinforced Polymer Composites

The longitudinal compressive strength of UD FRP composites is much lower than their tensile strength. Experiments conducted on UD CFRP composites have shown their longitudinal compressive strength is on average 60-70% lower than their tensile strength [20]. Such a significant reduction in strength between tensile and compressive loading is due to the change in failure modes. In tension a UD FRP composite fails primarily in fiber rupture which is governed primarily by the ultimate strength of the fiber used. In compression a UD FRP composite can fail in a variety of modes, such as fiber micro-buckling [21], [22], fiber crushing [23], [24], fiber kinking [25]–[30], and matrix cracking and splitting [23], [29].

Fiber micro-buckling is perhaps the most widely studied failure mode and is self-explanatory in that it occurs when the individual fibers embedded in a polymer matrix experience a loss in stability and elastically buckle. Micro-buckling is mainly controlled by the matrix shear stiffness. One of the earliest theories for the longitudinal compressive strength of UD FRP composites was an elastic micro-buckling theory developed by Rosen. Rosen assumed 2-D perfectly aligned fibers in a linear elastic matrix, a long buckle wavelength, and very high fiber shear stiffness relative to the matrix. An energy method was then used by Rosen to derive the below expression shown in Equation (8) where the fibers have buckled in a so-called shear mode, as shown below in Figure 11.

$$\sigma_c = G_m \frac{1}{1 - V_f} \tag{8}$$

The variable σ_c is the composite compressive strength, G_m is the shear modulus of the matrix, and V_f is the fiber volume fraction. The above result should actually be interpreted as:

$$\sigma_c = G_{12} \tag{9}$$

Where G_{12} is the effective longitudinal shear modulus of the composite and the right hand-side of Equation (8) is an approximation of G_{12} [6], [31]. The analytical expression in Equation (8) has been shown to greatly overpredict real compressive strengths of UD FRP composites. However, it is important to consider Rosen's work since most compressive failure theories have been built off his in some way.
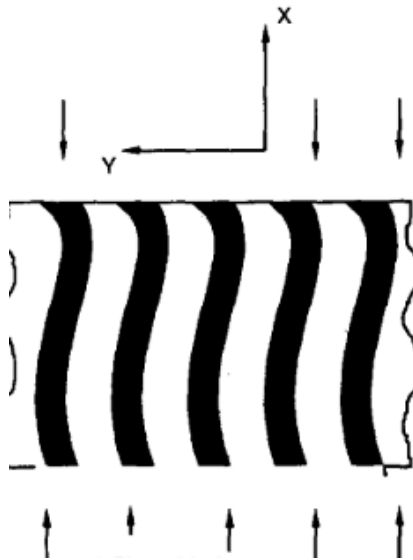
Figure 11: Shear mode micro-buckle failure as described by Rosen [21]

Fiber crushing is when the fibers reach their ultimate strength and rupture before any buckling can occur. This failure behavior is expected to dominate composites where the fiber is weak in compression such as Kevlar [29]. This failure mode is almost entirely influenced by the fiber mechanical properties; the matrix properties have little influence.

Matrix cracking and splitting occurs in composites with either strong fibers, brittle matrices, and weak fiber/matrix interfaces, or a combination of these factors. Matrix cracking and splitting is controlled by the fracture toughness of the matrix material and is also strongly affected by the mismatch in Poisson's ratio between the fiber and matrix [29]. Matrix cracking and splitting can in some cases lead to other failure modes such as micro-buckling and kink banding due to the local instability caused by the loss of support around the crack [32].

Fiber kinking has been shown to be the dominant mode for UD CFRP composites under longitudinal compression [23], [27], [29], [30]. Fiber kinking is a localized shear deformation of the matrix accompanied by eventual fiber fracture. It is sometimes considered to be a final consequence of micro-buckling.

<u>Mechanics of Fiber Kinking</u>

Many researchers have attempted to gain a fundamental understanding of the physics of fiber kinking through experimentation, and micromechanical modeling [23], [30]. All these studies agree that the main factors affecting fiber kinking are fiber misalignment and matrix yielding. It has also been shown that kink band formation can be separated into three distinct phases:

1. **Initiation**: Fibers with an initial misalignment φ_0 micro-buckle where they undergo a large rotation γ that adds to the initial misalignment within a band. The rotation of the fiber results in large shear stresses developing in the matrix causing local matrix yielding and further fiber rotation.

2. **Propagation**: The kink band propagates transversely to the fiber direction across the composite specimen. This propagation moves across the lamina at an angle β known as the propagation angle. Experiments have reported that β lies between 10° and 30° for CFRP lamina.

3. **Broadening**: The kink band has propagated completely across the FRP lamina transverse to the fiber direction and begins to "broaden" along the fiber direction.

Three geometric features that are important to the fiber kinking process are the total fiber rotation $\varphi_0 + \gamma$, propagation angle β, and band width w_{kb}, (Figure 12). These geometric variables are also seen in CFRP compression test experiments performed as seen in Figure 13.
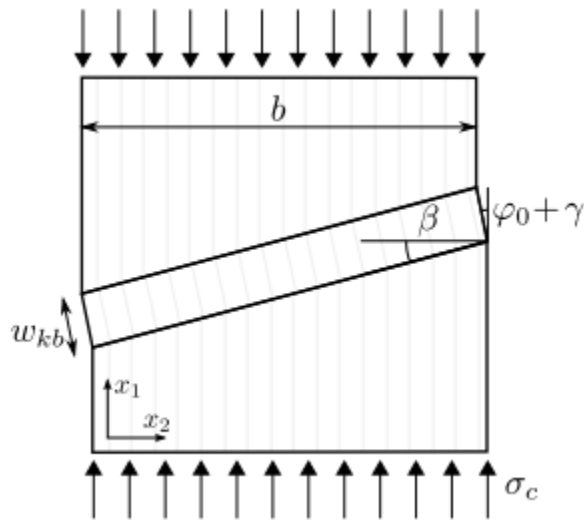
Figure 12: Geometric idealization of fiber kinking [33]
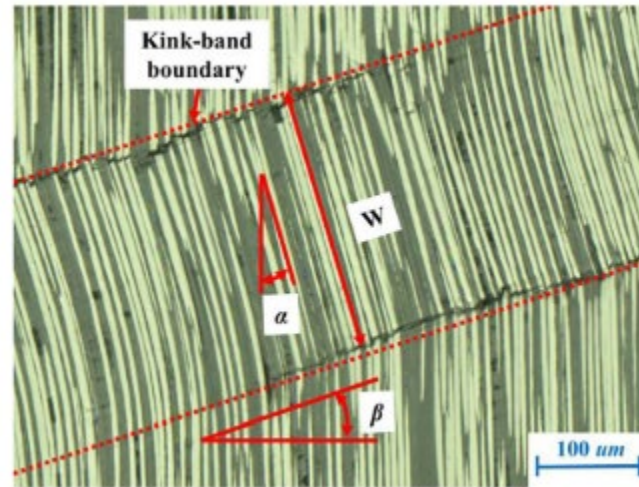
Figure 13: Micrograph of kink-band geometry from a compressive failure of a CFRP lamina [30]

The sequence in which fiber kinking takes place can also be described in terms of stress vs. strain. A typical stress-strain curve for fiber kinking follows a classic buckling curve where there is an initial linear elastic region which ends at a peak load, followed by an instability that causes a loss of load, finally the stress levels out to a residual stress σ_r in which the kink-band propagates (Figure 14).
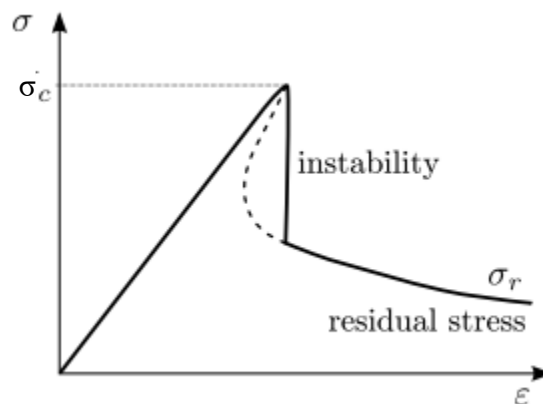
Figure 14: Typical stress-strain curve for fiber kinking [33]

Analytic Models of Fiber Kinking

Numerous analytic models have been proposed over the years for fiber kinking. Most analytical models proposed have been modifications of the seminal work of Rosen. Argon extended Rosen's work, and found that composite manufacturing techniques introduce regions of fiber misalignment. Compressing these areas with fiber misalignment leads to the development of local shear stresses that when they yield, they cause the composite shear modulus to decay creating a local instability.   To account for this phenomena Argon added in effects from initial fiber misalignment φ_0, and incorporated perfectly plastic shear behavior with the addition of a shear yield stress of the composite lamina term τ_y, as shown below in Equation (10) [34].

$$\sigma_c = \frac{\tau_y}{\varphi_0} \tag{10}$$

The Argon model assumes kinking occurs at $\beta = 0$ and that additional rotation of the fibers γ cannot develop in the fibers until the critical compressive stress is reached. Argon was the first to consider micro-buckling and fiber kinking to be two separate failure mechanisms. However, even accounting for yielding and initial imperfections Equation (10) still overpredicts experimental values as much as 2.5 times [29].

Budiansky extended Argons work by including the non-linear shear response of the matrix [35]. He first considered an elastic-perfectly plastic lamina with yield strain $\gamma_y = \frac{\tau_y}{G_{12}}$ under longitudinal shear with inextensible fibers and assumed the kink band propagated at an angle $\beta = 0$. Equilibrium was then used to derive the below Equation (11) for composite compressive strength.

$$\sigma_c = \frac{\tau_y}{\gamma_y + \varphi_0} = \frac{G_{12}}{1 + \frac{\varphi_0}{\gamma_y}} \tag{11}$$

An interesting note is that if $\varphi_0 = 0$ then Equations (11) simplify to Equation (8).

Barbero derived an expression to predict the compressive strength of FRP composites using the principal of total potential energy and modeling the shear response τ of a composite as Equation (12) [36].

$$\tau = \tau_u \, tanh\left(\frac{G_{12}\gamma}{\tau_u}\right) \tag{12}$$

Where τ_u is the longitudinal shear strength of the composite. The expression Barbero derived for composite compressive strength was extensive so he proposed a numerical best fit instead which is given in Equation (13).

$$\sigma_c = G_{12}\left(\frac{\chi}{0.21} + 1\right)^{-0.69} \tag{13}$$

Where $\chi = \frac{G_{12}\tilde{\varphi}_0}{\tau_u}$ with $\tilde{\varphi}_0$ being the standard deviation of φ_0 in the composite. It is important to note that Equation (13) is not an empirical formulation but rather an approximation of a more complex analytical formula.

All the previously mentioned fiber kinking theories and expressions have neglected the geometry of the fiber such as length and diameter in their models which experimentation has shown to have an effect composite compressive strength [23], [37]. To account for these discrepancies Lagoudas and Saleh developed and energy-based

formulation which includes both fiber length L, and fiber diameter d [38]. Lagoudas and Saleh's work was unique up until this point in that both microscale and macroscale factors were considered in Equation (14).

$$\sigma_c = w_{kb}\sqrt{\frac{2V_f E_1}{\pi dL}} \tau_{ym}\varphi_k \tag{14}$$

Where E_1 is the composite lamina modulus in the fiber direction, τ_{ym} is the shear yield stress of the matrix, and φ_k is the angle of the kinked fibers. One drawback of this analytical expression is the reliance on post-failure data that is dependent on other initial conditions such as kink band width and angle of the kinked fibers. This means to large amounts of data with various initial conditions are needed to use this expression effectively.

Pimenta et al used a discrete micromechanics approach to solve the composite compressive strength problem analytically [39]. This contrasts with all the previously discussed analytical models that homogenized the fiber kinking process to a mesoscale. Pimenta's model was derived using equilibrium of a misaligned fiber, the fiber was embedded in an elastic perfectly-plastic matrix, and is given below as Equation (15):

$$\sigma_c = \tau_y \frac{G_{12}^{2D} d + \frac{\pi^2}{L^2} E_f I_f}{\tau_y + \pi \frac{y_0}{L} G_{12}^{2D}} \left(\frac{V_f^{2D}}{A_f}\right) \tag{15}$$

Where the subscript f indicates quantities associated with the fiber and G_{12}^{2D} is the shear modulus of a composite lamina under a 2D assumption, y_0 is the maximum amplitude of the initial fiber imperfection, L is the length of the fiber imperfection, and I is the moment of inertia. Interestingly, Equation (15) considers properties of the fiber which

historically has not been the case, the above formulations mainly focus on properties of the matrix material to determine compressive strength. One drawback of Equation (15) is its reliance on the 2-D assumption which inherently adds error into the reality of 3-D compressive failure of composites.

A commonality between all the above-mentioned analytical models is their emphasis on the importance of shear effects on composite compressive strength. This suggests that at the micro-level a UD FRP composite deforms primarily in shear. This contrasts with Euler beam theory in which shear effects are neglected because shear stiffness is so much higher than bending stiffness. In micromechanical composite compression, the opposite is true and fiber bending is neglected in the above models and only shear is considered.

While analytical models have been of great importance to understanding the fundamental physics of FRP composite compressive failure, they are severely limited in their ability to analyze different structural configurations, and most only describe the moment of failure and cannot describe or predict pre- and post-failure response. For these reasons, most recent research on the fiber kinking failure mechanism has been with numerical methods, specifically the finite element method (FEM).

Numerical Models of Fiber Kinking

In recent years with advances in computational power and efficiency, numerical modeling using FEM has become a popular choice for researchers to examine the physical mechanisms behind the fiber kinking phenomena. By discretely modeling the fiber and matrix individually in an RVE or RUC and accounting for various nonlinearities that arise

out of the geometry and material the fiber kinking failure process can be accurately modeled. Numerical solutions offer insight into the different stages that occur in the fiber kinking process that would otherwise be hard to capture in an experiment due to how sudden and quick compressive failures happen in CFRP composites. They also offer a cost effective and quick way to perform parametric studies to determine different parameters effects on the fiber kinking process. Historically, micromechanical modeling of fiber kinking can be split into two groups, 2-D representations and 3-D representations.

2-D Numerical Models: The first attempts at discrete modeling of fiber kinking were done using a 2-D representation of the fiber and matrix material because of the savings in computational cost and the limits of earlier computers. One of the first micromechanical models developed to simulate fiber kinking was by Kyriakides et al. [37], The model consisted of alternating layers of linear elastic fibers and an elasto-plastic matrix as seen in Figure 15. The matrix material was modeled with J_2-flow theory, otherwise known as the Maxwell-Huber-Hencky-von Mises yield criterion to account for the post-yielding response experienced in fiber kinking. A sinusoidal extrusion of the fiber was used in Kyriakides paper to simulate a fiber misalignment imperfection; this has become the preferred method to introduce geometric imperfections into non-linear fiber kinking analyses. This was also one of the first models to predict the sequence of deformation mechanisms that constitute fiber kinking.
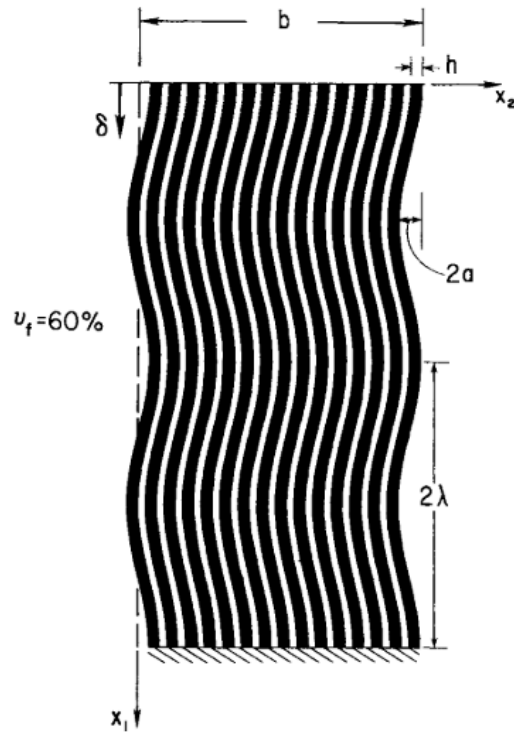
Figure 15: Geometric Representation of Kyriakides et al. FEM model at a volume fraction of 60% with the dark stripes representing fibers and the white representing the matrix [37].

Pimenta et al. [27] used a 2-D model like the one described above with multiple layers of alternating fiber and matrix. The model used a non-uniform fiber imperfection with only an imperfection on one side of the model to study the propagation of the kink band through the model. These models also made use of continuum damage mechanics to study the effect of damage on kink band evolution. The authors found that the numerical models suggested kink-band formation is matrix strength (and not matrix toughness) dominated.

Gutkin et al. [26] developed a single fiber model, as seen in embedded in matrix material to analyze failure envelopes of UD FRP composites in combined longitudinal compression and in-plane shear. This model differs from the previously mentioned ones in

that PBCs were used to represent the bulk composite as a periodic array and reduce computational costs instead of explicitly modeling the bulk material as multiple fibers.
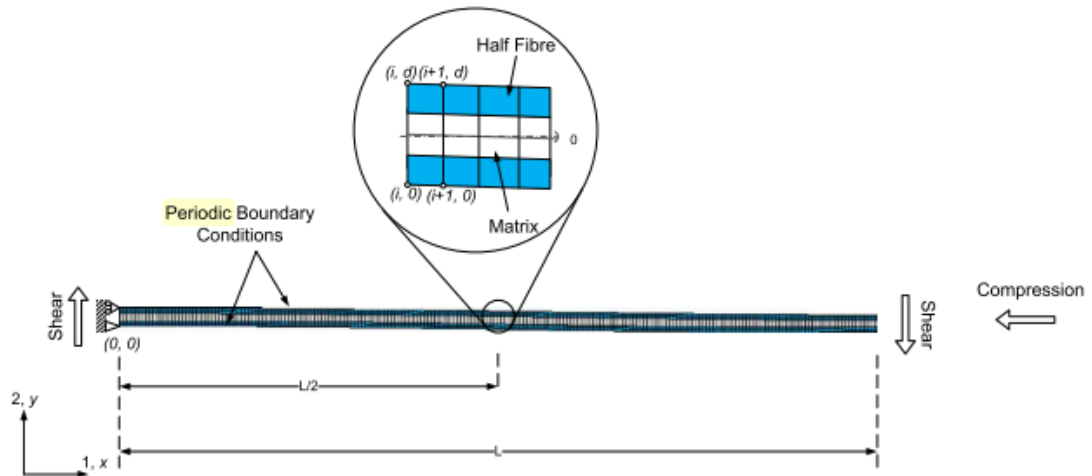
Figure 16: Gutkin et al. FEM micromechanical model: 2-D single fiber geometry, boundary conditions, and loading [26].

This model showed two separate failure mechanisms in shear driven fiber failure that transitions to kink-band formation, which was then verified with complementary experimental research. An interesting implication of PBCs is that the kink band angle β is equal to zero since when the RUC buckles and kink bands it propagates instantaneously. Gutkin et al. found that this assumption has a negligible effect on the compressive strength results by comparing the single fiber model to a model containing 100 fibers.

The interaction between fiber kinking and fiber-matrix debond (splitting) was investigated by Prabhakar and Waas [40]. Using a 2-D multifiber model with cohesive zone elements in between the fiber and matrix. It was found that mode-II fracture toughness had a significant effect on the compressive strength of a composite laminate whereas mode-I fracture toughness's effect is negligible.

The effect of fiber volume fraction on the compressive strength and compressive stiffness was investigated by Zhou et al. [41]. A 2-D model consisting of 60 fibers that incorporated interface failure at the matrix and fiber interface with cohesive zone elements and fiber fracture with a continuum damage model based on the maximum stress criterion. The authors found that while compressive strength increases linearly with volume fraction, the compressive strength will increase up to 60% fiber volume fraction then decrease because of premature fiber-matrix interface failure.

One drawback in using a 2-D representation is the ambiguity in the volume fraction of the composite being represented. For instance, the 2-D fiber volume fraction could equal the actual 3-D fiber volume fraction, $V_f^{2D} = V_f^{3D}$; or the 2-D representation could represent an hexagonal fiber arrangement where $V_f^{2D} = \sqrt{\frac{2\sqrt{3}}{\pi} V_f^{3D}}$. It has been shown that if the hexagonal representation is being used then the 2-D representation gives a less conservative prediction of compressive strength [26]. Another drawback of a 2-D representation of kink-banding is the plane-strain assumption built into the models which can introduce artificial stiffness.

<u>3-D Numerical Models</u>: 3-D numerical models of fiber kinking naturally came after the 2-D models because of the increase in computational power needed for the added dimension. One of the first 3-D micromechanical FEM models was done by Hsu et al. [42] to determine the limitations of 2-D models. A hexagonal distribution of 60 linear elastic, isotropic fibers were used, as seen in Figure 17, the matrix was modeled in a similar manner to Kyriakides et al. [37] using J_2 flow theory. The inclusion of fiber

misalignment into the 3-D model was implemented as a 2-D sinusoidal curve in a similar manner as Kyriakides et al.
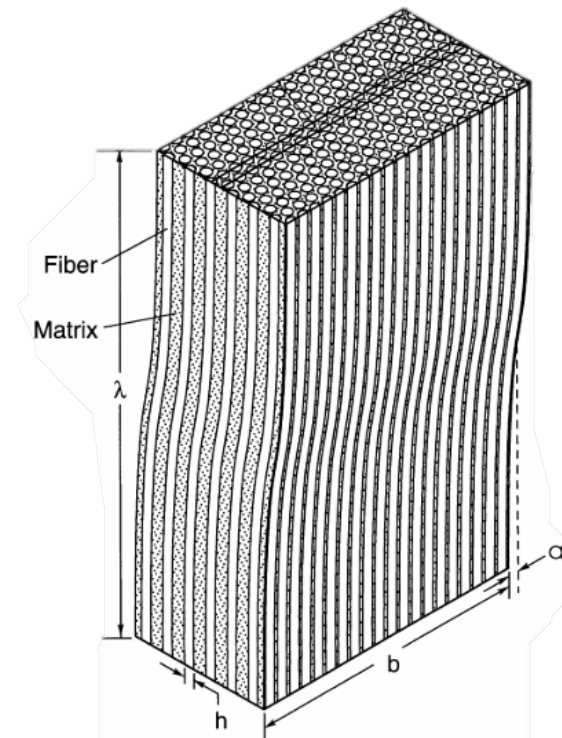
Figure 17: Geometry definition of the micromechanical model used by Hsu et al. [42].

The authors showed that 2-D and 3-D representations gave similar results in predicting the critical compressive strength of FRP composite materials. An interesting observation by the authors is the inability of either the 2-D or 3-D models in accurately modeling the post-peak load response and determining the residual stress σ_r. A follow-up study by Vogler et al. [43] used the same 3-D model as Hsu et al. [42] but modeled the matrix using a Drucker-Prager plasticity model to account for the pressure sensitivity exhibited by many thermoplastic polymers. The new model showed good agreement with experimental observations of the post-peak load response and residual stresses indicating

that hydrostatic pressure is a factor in kink-band propagation in composites with a thermoplastic matrix.

Yerramalli and Waas [44] developed a 3-D cylindrical model consisting of 37 fibers, as shown below in Figure 18 to study the effect of fiber size on fiber kinking failure. The matrix was once again modeled using J_2 flow theory. A study was carried out comparing orthotropic fibers vs. isotropic fibers, it was determined that orthotropy had little effect on peak stress but did lower the residual stress. PBCs were not used in this study because they are a first-order method and therefore size cannot be accounted for, only ratios i.e. volume fractions. The authors found that the compressive peak load decreased with smaller fibers because they fracture earlier than larger ones which prematurely initiated kink band failure.
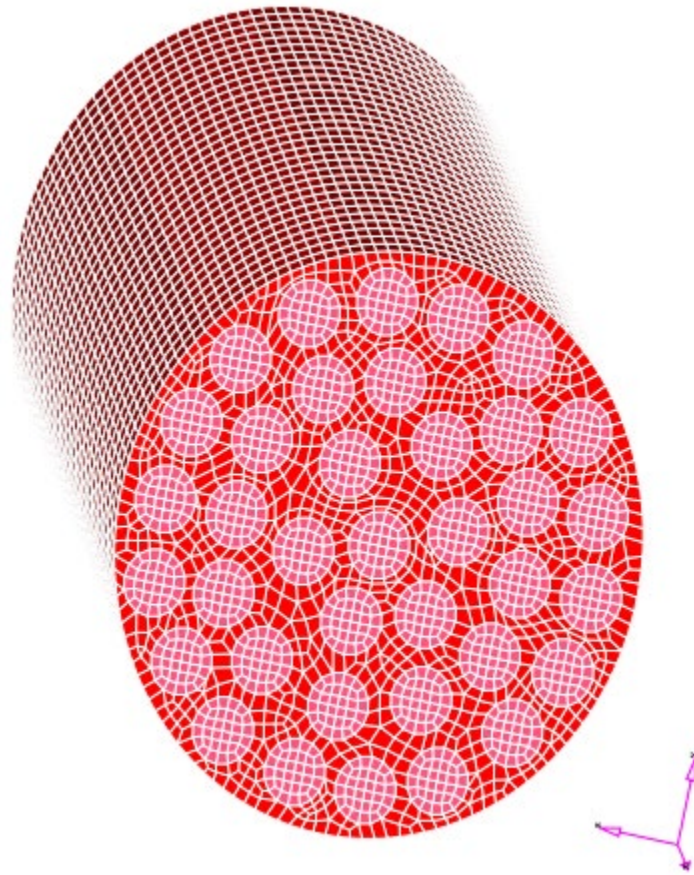
Figure 18: Geometry and meh of 3-D micromechanical model developed by Yerramalli and Waas [44].

Barulich et al. [45] used a 3-D single fiber RUC model (See Figure 19) with a sinusoidal extrusion to simulate fiber misalignment. Both fiber and matrix were isotropic with the matrix plasticity being modeled using J_2 flow theory. The authors conducted a parametric study of fiber misalignment angles and found that defect sensitivity was only high for small misalignment angles. It was also determined in this study that fiber volume fractions influence on peak compressive load decreased with increasing fiber misalignment.

Figure 19: Geometry and mesh of a single fiber RUC model with sinusoidal imperfection used in Barulich et al. [45].

Recently, Naya et al. [46] investigated the differences in fiber kinking results between a multifiber RVE (see Figure 20) and a single fiber RUC and compared the results with physical experimentation. Both the multifiber RVE and single fiber RUC modeled the carbon fiber as linear elastic transversely isotropic solids, the matrix was modeled using a modified Drucker-Prager plasticity model with a damage variable to account for the polymers quasi-brittle behavior. The authors found that the single fiber RUC provided just as accurate of answers as the multifiber RVE for pre-peak load response i.e. compression elastic modulus and compression strength. The multifiber RVE was also able to give accurate predictions for post-peak load response such as kink-band angle and residual stress whereas the single fiber could not.
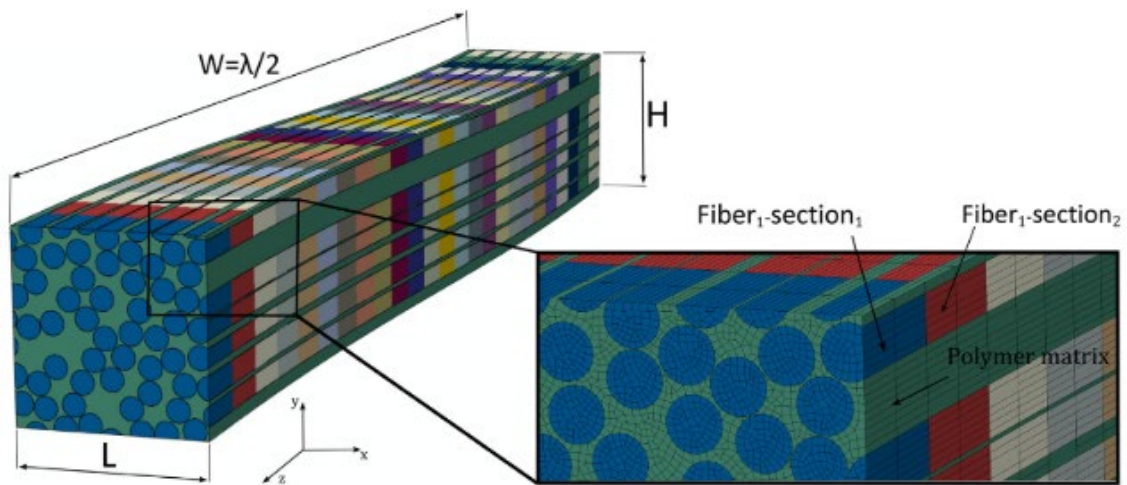
Figure 20: Geometry and mesh of a multifiber RVE used by Naya et al to investigate post-peak load response of FRP composites [46].

Buckling Solution Methods

The majority of compressive failures of composites involve buckling [29]. To be able to solve for buckling failures in these analyses specialized analysis methods within FEM must be used. To solve buckling procedures either linear or nonlinear analysis can be used with pros and cons to each.

Linear Buckling Analysis

In FEM Linear Eigenvalue Buckling Analysis (EBA) is the primary solution method to Linear Buckling problems. EBA is a linear perturbation procedure and is generally used to estimate the critical elastic buckling (bifurcation) load of structures as well as the mode shapes that the structure will most likely collapse into. Eigenvalue analysis is most accurate if the structure being analyzed is a "stiff" structure meaning the structure carries its loads mainly through axial or membrane action rather than bending action. However, even when the behavior of a structure is non-linear before collapse an

EBA can provide useful estimates of collapse mode shapes as well as a first estimate of the critical buckling load of a structure.

In an EBA problem, a base load that was applied before the solution procedure is incrementally increased until a series of loads are found which satisfy Equation (16).

$$([K] - \lambda[K_s])\{v\} = 0 \qquad (16)$$

Where $[K]$ is the stiffness matrix, $[K_s]$ is the stress stiffness matrix, λ is the eigenvalues and $\{v\}$ is the eigenvectors [47]. The applied loads can be pressures, concentrated forces, displacements, and/or thermal loads.

The eigenvalue buckling loads calculated from an EBA are relative to the base state of the model and will be output as a multiplier of the prescribed base load. The critical buckling load predicted is then equal to a load multiplier multiplied by the base load. Normally the first buckling load predicted by an EBA is of most interest. Another output of EBA is the buckling mode shapes that are associated with their respective critical buckling load. Buckling mode shapes can be physically interpreted as the general shape in which the structure will collapse into and are calculated from the eigenvectors obtained. An important thing to note is that the buckling mode shapes are normalized vectors and do not represent the actual displacements present at the critical buckling load. Often, the first buckling mode shape of an EBA is used to introduce a geometric imperfection into a structure to be used for nonlinear analysis. Sometimes an EBA will produce a negative value for the critical load which physically means the base load applied needs to be reversed to induce buckling of the structure.

An obvious drawback of Linear EBA is that it is inherently nonconservative since it approximates the model as a perfect structure with no imperfections. Also, since a model's response in EBA is defined by the linear elastic stiffness in the original state, all nonlinear or inelastic material properties are ignored adding to the potential error. Finally, Eigenvalue Buckling Analysis only gives information about the state of the structure at its critical buckling load assuming that the pre-buckle path is trivial and is unable to determine any information about the post-critical path severely limiting the information that can be obtained from this type of analysis.

Nonlinear Buckling Analysis

The Modified Riks method is a common and powerful numerical analysis method used to incorporate nonlinear effects into an FEM analysis. The Modified Riks Method is generally used for geometrically nonlinear collapse of structures and can incorporate nonlinear materials and boundary conditions. It can also solve problems that exhibit both snap-through and snap-back instabilities, as shown in Figure 17. The Modified Riks Method depends on the load being proportional meaning that all applied loading magnitudes vary by a single scalar parameter. All prescribed initial loads are ramped from the initial load to the reference values specified so that the current load magnitude can be calculated by Equation (17)[47].

$$P_{total} = P_0 + \lambda\left(P_{ref} - P_0\right) \tag{17}$$

Where P_0 is the initial load, λ is the load proportionality factor, P_{ref} is the reference load vector, and P_{total} is the current load magnitude. λ is found as part of the solution.
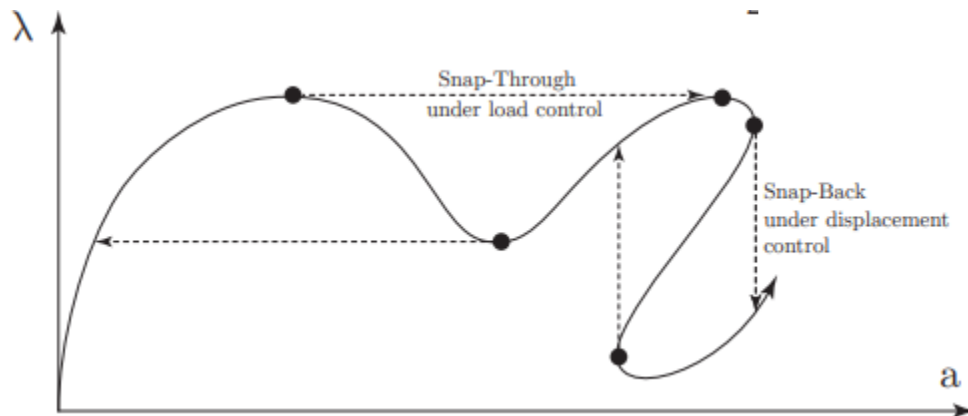
Figure 21: Illustration of a system that exhibits both snap-through (unstable under load control) and snap-back (unstable under displacement control)[48]

The Modified Riks Method treats the load magnitude as an additional unknown and solves displacement and loads simultaneously. Because loads are also being solved for in this analysis method another quantity must be used to measure the progress of the solution, in ABAQUS the arc-length along the static equilibrium path in load-displacement is used [47].

To better describe how the Modified Riks Method algorithm works in ABAQUS, first variables need to be defined. Let P^N be the loading pattern with N=degrees of freedom within the model. λP^N is the actual load state in the analysis with λ being defined previously, and u^N being the displacements at that time. Then the solution space is scaled such that the dimensions are approximately equal in magnitude so the load equals $\lambda \tilde{P}^N$ where $\tilde{P}^N$ is the normalized load vector P^N and the displacements equal $\tilde{u}^N$ where $\tilde{u}^N$ is the normalized displacement vectors. The solution path is then a set of equilibrium points that can be described by the vector $(\tilde{u}^N, \lambda)$ which can be seen in Figure 18.
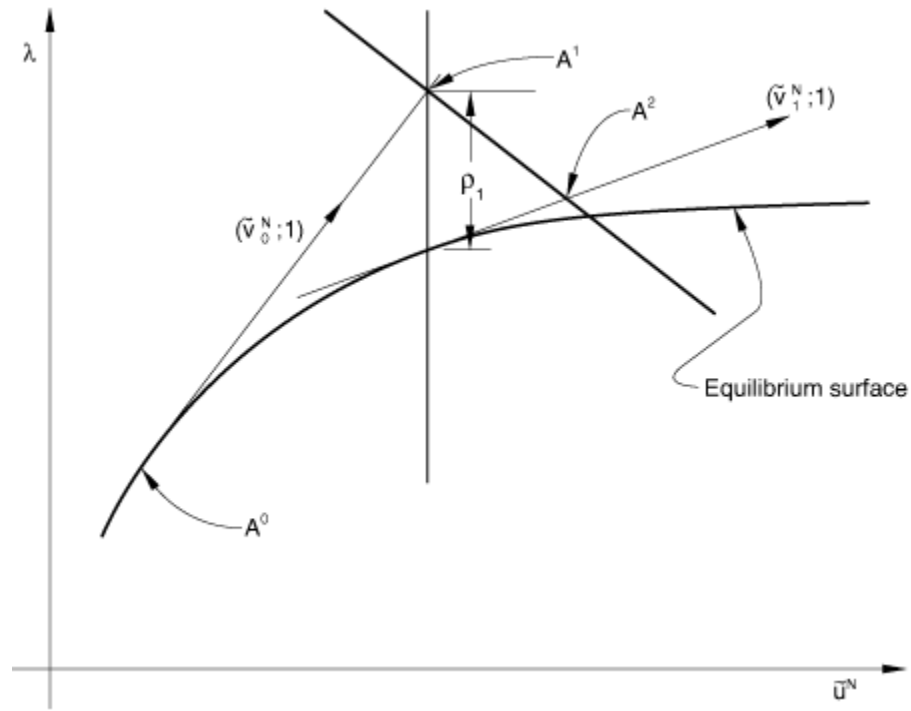
Figure 22: Graphical representation of the Modified Riks Algorithm in ABAQUS [47].

Now suppose the solution has developed to a point $A_0 = (\tilde{u}_0^N, \lambda_0)$, then Equation (18) is solved to arrive at point A_1.

$$K_0^{NM} v_0^M = P^N \tag{18}$$

Where K_0^{NM} is the tangent stiffness, and v_0^M is the displacement vectors at that solution step. The increment size A_0 to A_1 is chosen from a specified path length Δl, in the solution space. The value for Δl is initially specified by the user and is subsequently automatically adjusted by ABAQUS's load incrementation algorithm [47]. Once the point A_1 is found the solution is corrected onto the structures equilibrium path in the plane passing through A_1 and orthogonal to the $\tilde{u}_0^N$ axis by an iterative procedure detailed below:

- Initialize: $\Delta\lambda_i = \Delta\lambda_0$, and $\Delta u_i^N = \Delta\lambda_0 v_0^N$

- For $i = 1,2,3$, etc.

o Form I^N, K^{NM}, which are the internal forces at the nodes

$I^N = \int_V \beta^N : \sigma dV$ and $K^{MN} = \frac{\partial I^N}{\partial u^M}$ at the state $A_i(u_0^N + \Delta u_i^N; \lambda_0 + \Delta \lambda_i)$

where β is the strain-displacement matrix and σ is the internal stress

o Check equilibrium: $R_i^N = (\lambda_0 + \Delta \lambda_i)P^N - I^N$

If all components of R_i^N are determined to be sufficiently small, the increment has converged, if not proceed.

o Simultaneously solve: $K^{MN}\{v_i^M; c_i^M\} = \{P^N; R^N\}$

Where P^N and R^N are two load vectors and v_i^N and c_i^N are the two displacement vectors that are solved for.

o Next normalize the vector v_i^N to $(\tilde{v}_i^N; 1)$ and add it to $(\tilde{c}_i^N; \rho_i)$ where ρ_i is the projection of the scaled residuals $\tilde{R}^N$ onto $\tilde{P}^N$ so that the solution is moved from A_i to $A_{(i+1)}$ in the plane orthogonal to $(\tilde{v}_i^N; 1)$ as shown in Figure 18. This gives the equation:

$$\mu = -\frac{\tilde{c}_i^N \tilde{v}_i^N}{\tilde{v}_i^N \tilde{v}_0^N + 1}$$

And the solution is now $A_i(u_0^N + \Delta u_i^N + c_i^N + \mu v_i^N; \lambda_0 + \Delta \lambda_i + \mu)$

o Update for the next iteration:

$$\Delta u_{i+1}^N = \Delta u_i^N + c_i^N + \mu v_i^N$$

$$\Delta \lambda_{i+1} = \Delta \lambda_i + \mu$$

$$i = i + 1$$

Return to start of the for loop for the next iteration.

Much like Linear Eigenvalue Buckling Analysis, the initial load applied can take many forms such as concentrated force, thermal load, pressure, surface traction, or displacements [47]. Displacement control with the Modified Riks Method tends to converge faster than load control.

One key difference between model setup of linear and nonlinear buckling analyses is in a linear analysis a perfect structure is analyzed and theoretical bifurcation loads are found. However, in a nonlinear analysis an imperfection must be introduced into the model to induce buckling otherwise the structure will yield and be crushed with a perfectly concentric load. This imperfection can take many forms, either as an element with slightly altered material properties, or a unit load that is applied laterally to initiate buckling in the model. One very common method is to use the first mode shape of a Linear Eigenvalue Buckling Analysis as a geometric imperfection in the structure. Another powerful benefit to the Modified Riks Method is that it provides information about the post-critical path of a buckled structure allowing analysis of post-failure responses.

A disadvantage of the Modified Riks Method is the increase in computational time and power it takes to obtain a solution due to it being an iterative procedure. Nonlinear Buckling Analyses also tend to be sensitive to the initial conditions of the model being analyzed producing very different results with only a small variation in the initial condition. This means to accurately use nonlinear analysis methods many simulations should be run to fully quantify the effect various initial conditions and nonlinearities will have on the solution.

MODEL DEVELOPMENT

Model Geometry

A single fiber RUC was used to accurately model the effect that fiber shape has on compressive strength of CFRP composites. The single fiber RUC was chosen because it has been proven that simple RUC models can accurately predict FRP composite properties if the correct boundary conditions are used (PBCs), while also being computationally efficient [26], [46].

Linear Analysis Geometry

The primary goal for the linear buckling analysis is validation of the PBCs for kink band analysis. To accomplish this a single circular fiber RUC model seen below in Figure 23 was used. The model can be fully defined by the volume fraction, width, and length.

$$V_f = 35\%$$

$$h = 10 \; \mu m$$

$$L = 675 \; \mu m$$

The geometry was created by sketching a 2-D model of the RUC face then extruding it outward along a straight line.
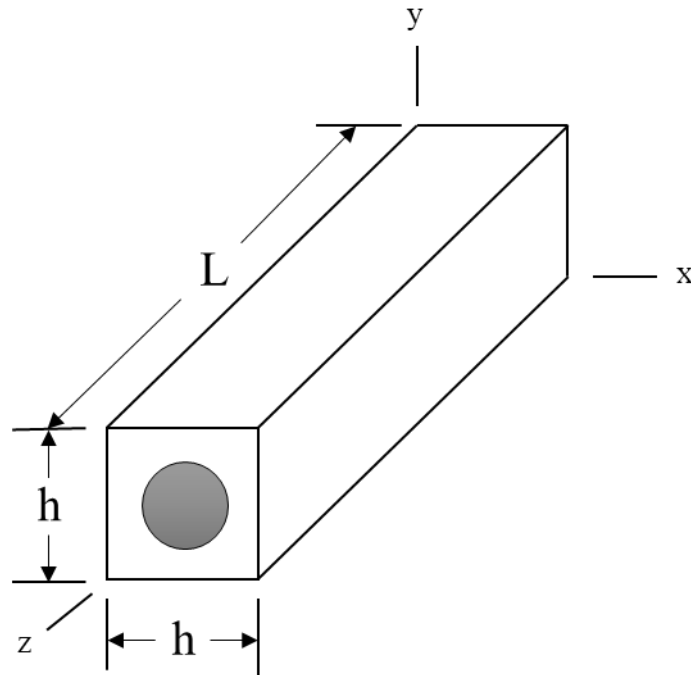
Figure 23: Geometry definition of linear elastic buckling analysis model.

In a unit cell analysis, the size of the fiber does not need to be known if the volume fraction is maintained, so the dimensions of the fiber is governed by its shape and dimensions of the model as a whole. The choice of length of the micromechanical model is not arbitrary and its significance will be discussed in greater detail later.

Non-Linear Analysis Geometry

In this work the primary goal is to investigate the effect that fiber shape has on the compressive response of UD CFRP laminas. To accomplish this two base RUCs were used. The first was a single circular fiber embedded in a square similar to linear model geometry described in the previous section, the second model was a single kidney-bean shaped fiber embedded in a square matrix. Both models had the same volume fraction and dimensions as the linear model geometry. The key difference between the linear model and the non-

linear models is the presence of a geometrical defect introduced in the form of a fiber misalignment defect described in the section below.

The aspect ratio of the kidney-shaped fibers was chosen to be 2.5 where the aspect ratio is defined as the major length divided by the minor width of the fiber as observed in the literature [49]. Different orientations of the fiber embedded in the RUC were used to account for the asymmetric shape of the kidney fiber RUC which would result in different buckling characteristics, therefore three orientations of the fiber in the RUC were analyzed to obtain a representative sample. The first orientation, Figure 19b, was 0° with the major axis of the fiber being vertical, second, the fiber was oriented at a 45° Figure 19c, finally, the fiber had a 90° orientation, Figure 19d, with the major axis being horizontal.
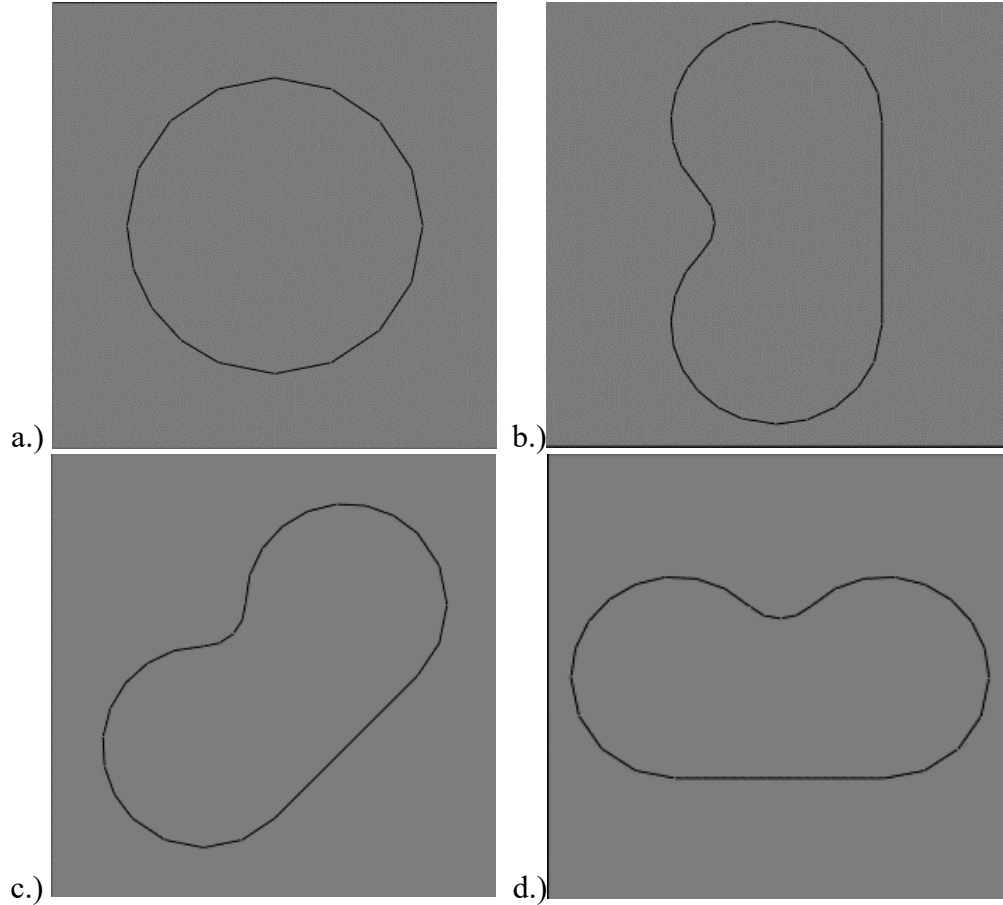
Figure 24: a.) Circular fiber RUC. b.) 0° kidney fiber RUC. c.) 45° kidney fiber RUC d.) 90° kidney fiber RUC.

Fiber Defect: Fiber misalignment was incorporated into the geometry by extruding the RUCs along the fiber direction as a half -wavelength sinusoidal spline to simulate a defect in the composite as shown in Figure 24 [50]. The z-axis was aligned with the fiber direction and the spline is described by the equation:

$$y = A \cos(\frac{\pi z}{L}) \tag{19}$$

Where *A* is the amplitude of the imperfection, and $2L$ is the wavelength of the imperfection. The misalignment angle α_0 of the initial imperfection can then be obtained by the equation:

$$\tan(\alpha_0) = \frac{\pi z}{L} \tag{20}$$

Five misalignment angles were chosen to run simulations at, 1°, 2°, 3°,4°, and 5°. The curves which represent these misalignments are shown in Figure 25. The implementation of the fiber misalignment into the RUC model can be seen below in Figure 26.
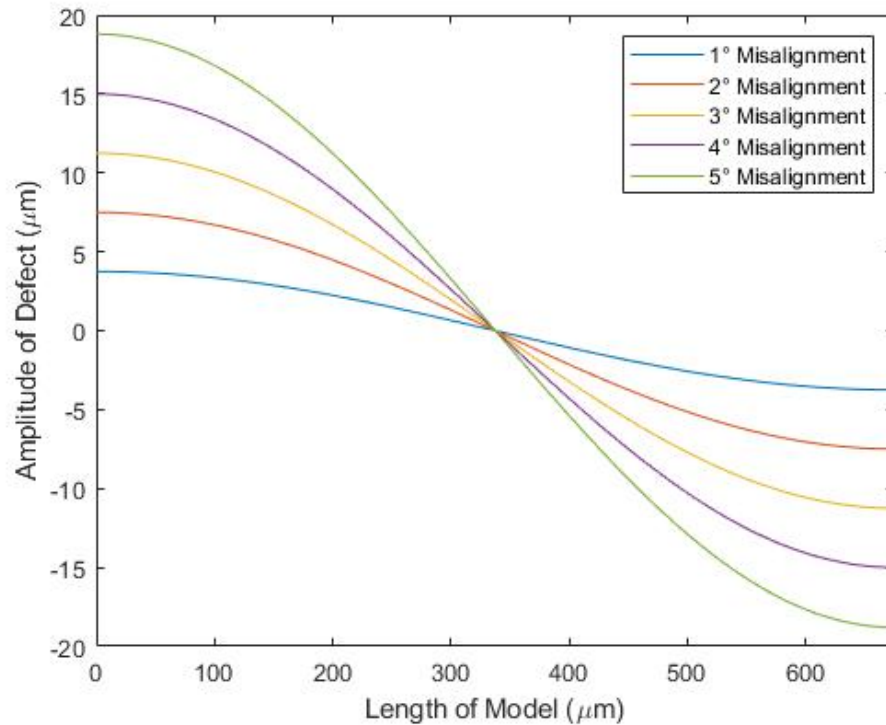
Figure 25: Five half-sine curves that the model is extrude along to represent varying degrees of fiber misalignment
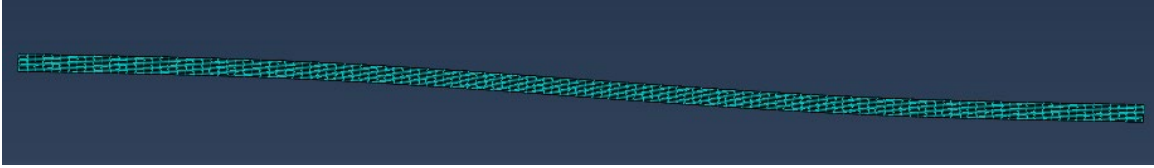
Figure 26: Example of a 4° fiber misalignment in the RUC model.

Model Length

The length of the RUC model has been shown to be important to the buckling response of composite micromechanics models. If the model is too short the model will predict an overly conservative estimate for composite compressive strength as well as not be able to capture all aspects of kink-band formation [26]. However, the model should not be too long to maintain computational efficiency.

Gutkin et al. [26] and Barulich et al.[45] both conducted parametric studies on their FE models and found that a fiber kinking results converge at approximately at a critical half wavelength corresponding to 75 times the fiber diameter used. Subsequent experimental results done Sun et al. [30] were in good agreement with the above mentioned parametric studies and found that the critical wavelength associated with kink band failure were on the order of 50-75 times the fiber diameter for CFRP composites.

From the results of the above studies the length L of the model analyzed, which corresponds to the half wavelength of the fiber, was determined to be approximately 75 times the diameter of the major axis of the kidney fiber, or 675 μm. This was determined to be the critical half wavelength and by increasing the model past this length the critical buckling load does not change and only increases computational time [26].

Boundary Conditions & Loads

A key aspect to any micromechanical analysis is the boundary conditions and loads applied to the model. For the RUC models used in this study the basic boundary conditions and loads remain the same and are illustrated below in Figure 27.

.
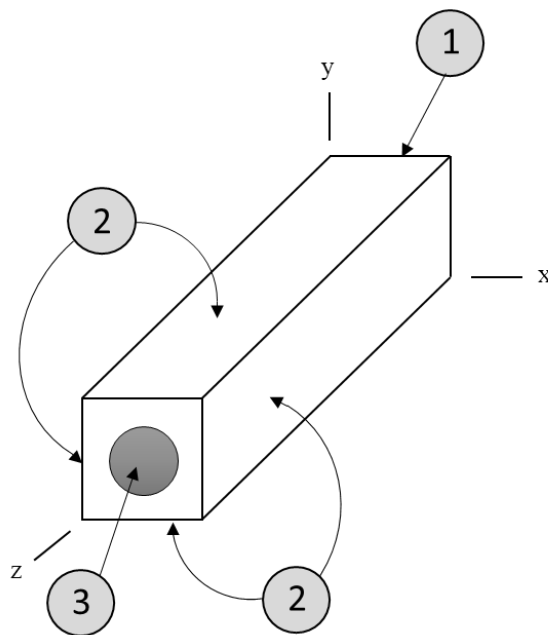
Figure 27: Location of RUC boundary conditions and applied loads

In Figure 27 The number indicates the Boundary Condition or load corresponding to:

1.) Rear Face of RUC: no z-displacement, pinned condition in x and y

2.) Lateral faces of RUC: PBCs applied

3.) Front Face of RUC: Incremental Compressive Displacement in the negative z-direction

The compressive load is applied as an incremental displacement to all nodes on the front z-face. Displacement control was used instead of load control for convergence purposes. The rear z-face of the RUC model was constrained from movement in the z-direction and one node in the middle of the fiber was constrained in the x- and y-directions to prevent free body motion. Finally, PBCs were applied to the lateral faces of the RUC model to approximate an infinite periodic array in both the x- and y-directions which is what a lamina effectively is compared to a single fiber.

Implementation Periodic Boundary Conditions in FEA

While the concept and theory behind PBCs is relatively simple, the practical implementation of them into a commercial finite element solver like ABAQUS is significantly harder. The purpose of this section is to give a conceptual understanding of how to effectively implement these boundary conditions into a micromechanical model. For ease of explanation a 2-dimensional model was used in this example.

Consider a 2-D RUC of a single fiber embedded in a square matrix as shown below in Figure 28 with PBCs applied to all four faces. For an FE model to have PBCs applied, it must first have periodic mesh topology. Periodic mesh topology means that for each node on the boundary of a unit cell there exists a paired node on the opposite boundary of the unit cell. For instance, in Figure 28 for a node on the positive x-face there is a node on the negative x-face that shares a y-coordinate with the first node and same goes for nodes on the y-faces.
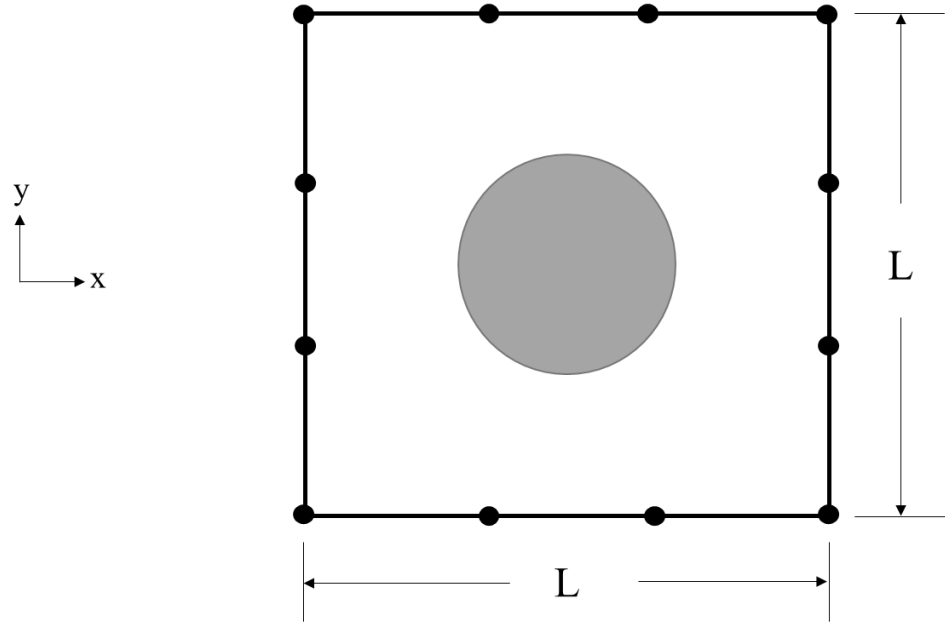
Figure 28: 2-D representation of a RUC with periodic nodes

Next recall, in the previous explanation of PBCs in the Theory portion of this thesis that in a finite element solver only the displacement condition of PBCs must be directly satisfied, and that the traction portion is naturally satisfied. For a simplified 2-D unit cell as used in this example, the displacement condition as seen in Equation (6) is implemented into the model as two equations, Equation (21) and Equation (22) shown below, one equation for each plane that has PBCs.

$$u_i(0, y) = u_{i'}(L, y) + U_x \tag{21}$$

$$u_j(x, 0) = u_{j'}(x, L) + U_y \tag{22}$$

Where U_x and U_y replace the ε_{ij} degrees of freedom in the periodic displacement condition and the i and i' denote the ith pair of nodes on opposing x-faces and j and j' denote the jth pair of nodes on opposing y-faces. Equations (21) and (22) are implemented

into an FE solver like ABAQUS using kinematic constraint equations that are made up of a linear combination of node displacement values. Since kinematic constraint equations in ABAQUS must always have 0 right-hand side, Equations (21) and (22) are rearranged into Equations (23) and (24).

$$u_{i'}(L, y) - u_i(0, y) + U_x = 0 \tag{23}$$

$$u_{j'}(x, L) - u_j(x, 0) + U_y = 0 \tag{24}$$

Equation (23) is then applied to each individual pair of nodes in the x-plane and Equation (24) is applied to each individual pair of nodes in the y-plane. U_x and U_y are introduced into the FE analysis as master nodes that are kinematically coupled to all the node pairs in their respective planes effectively creating an averaging effect that acts like the macroscopic strain ε_{ij}. The constraint applied on the degrees of freedom of the master nodes is dependent on the loading applied. For uniaxial deformation along the x-axis $U_x = (1,0)$ and $U_y = (0, u_y)$, with u_y meaning the master node U_y is unconstrained in that degree of freedom. The visual representation of the application of these constraint equations can be seen in Figure 29, and Figure 30 with the gold nodes representing the master nodes U_x and U_y.
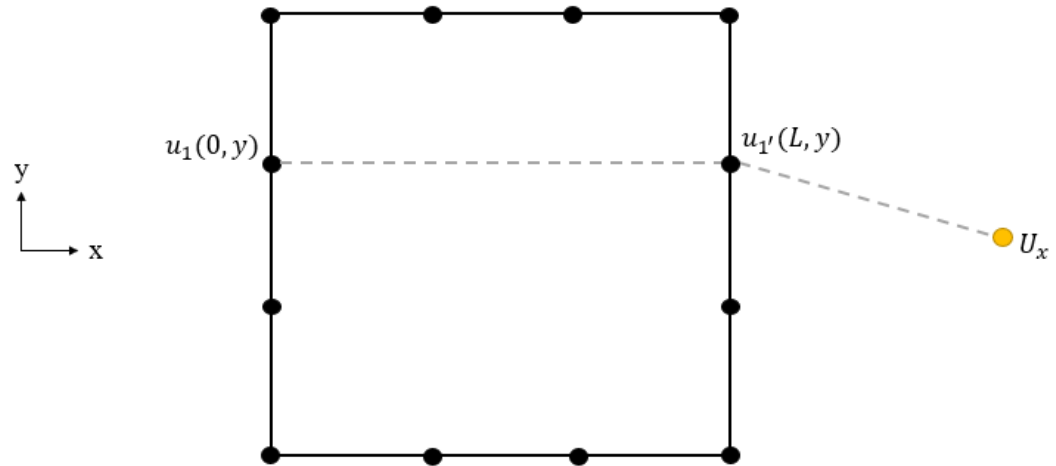
Figure 29: Visual representation of a single kinematic node constraint used to define the displacement condition in PBCs
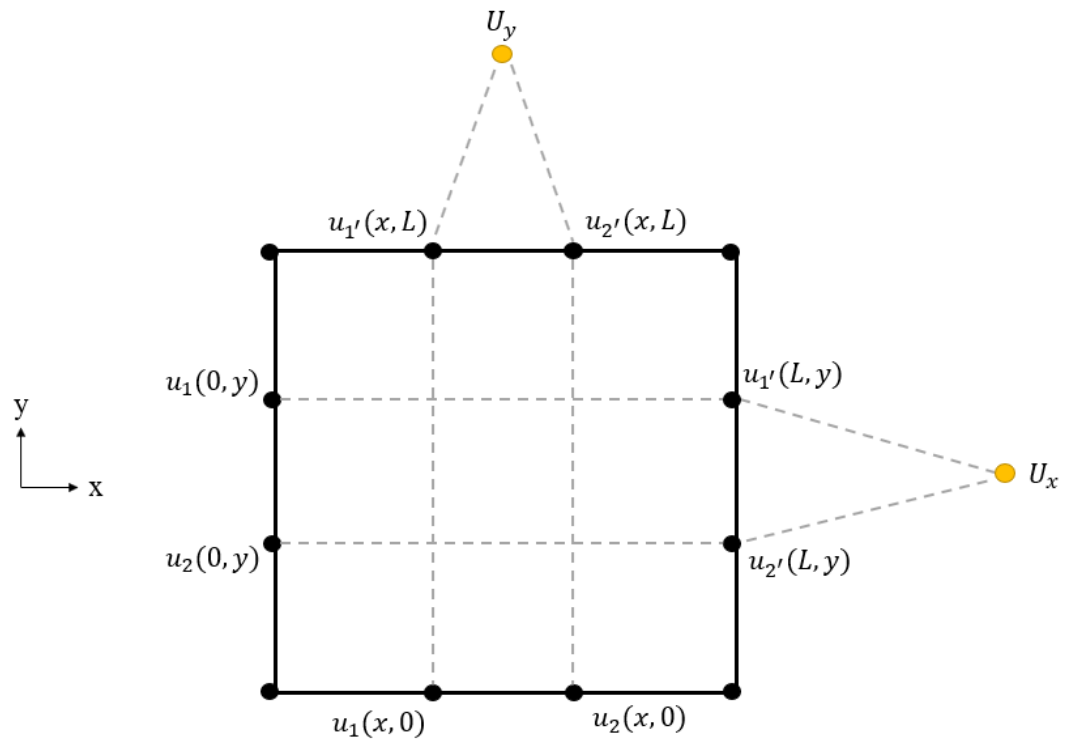
Figure 30: Visual representation of all interior kinematic node constraints used to define the displacement condition in PBCs

Since corner nodes belong to two faces the constraint equation for them becomes more difficult than the interior nodes because they would become over constrained if they were constrained in both directions. To deal with this problem the corner nodes are coupled to one another with the following equations.

$$u(0, L) - u(L, L) = -U_x \qquad (25)$$

$$u(L, L) - u(L, 0) = U_y \qquad (26)$$

$$u(L, 0) - u(0,0) = U_x \qquad (27)$$

By following Equations (25), (26), and (27) the corner nodes are satisfactorily kinematically constrained without being over constrained. A Python code used to automate the PBC implementation process into ABAQUS CAE for a RUC can be found in Appendix A.

<u>Mesh</u>

All finite element models were meshed with 3-D 8-node fully integrated iso-parametric linear brick elements (C3D8). The in-plane mesh size is set such that 10 elements along the edge length of the RUC and six elements through the thickness of the circular fiber. Example meshes of the circular and 0° kidney fiber can be seen in Figure 31 and Figure 32
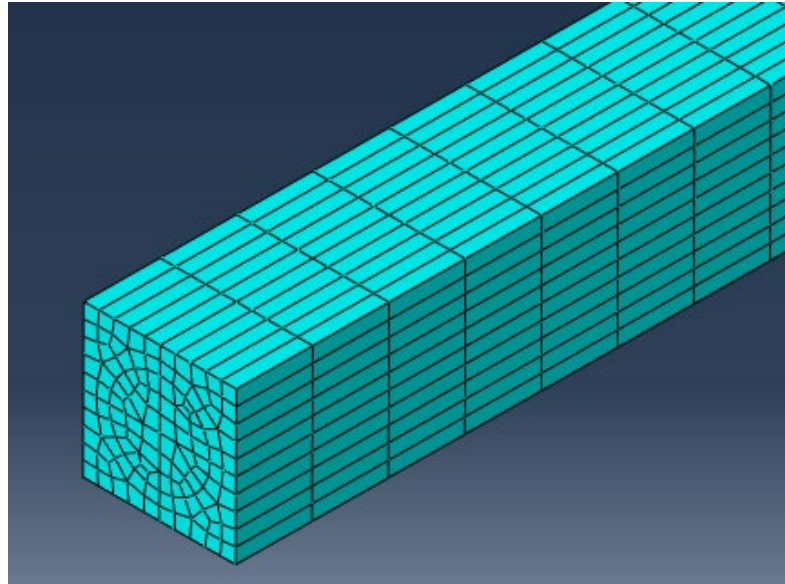
Figure 31: Meshed circular fiber RUC.
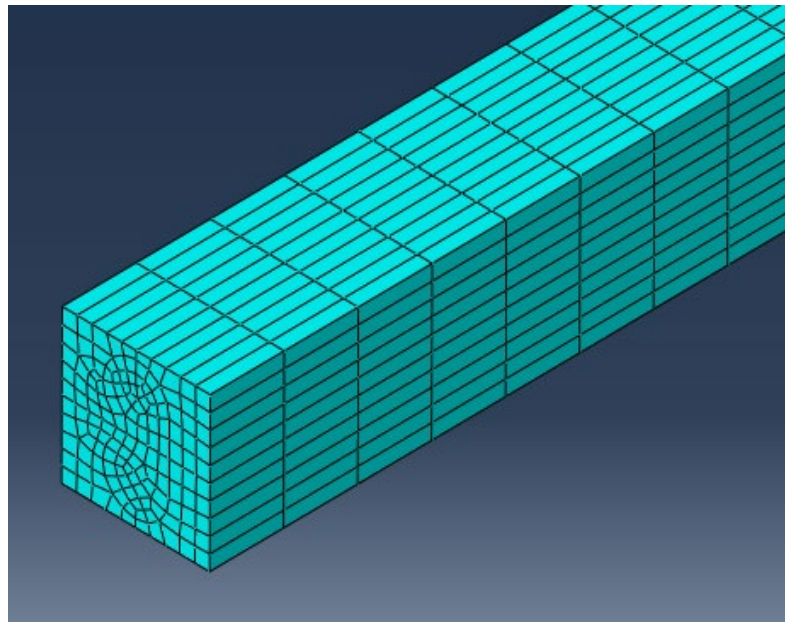
Figure 32: Meshed 0° kidney fiber RUC.

Mesh Sensitivity Study

A mesh sensitivity analysis was conducted using elements of decreasing lateral length. It was determined that the mesh converges at an element with a lateral length of 5

μm, as shown in Figure 25, which corresponds to an element aspect ratio of 5. The resulting

model mesh has 135 elements along its length.
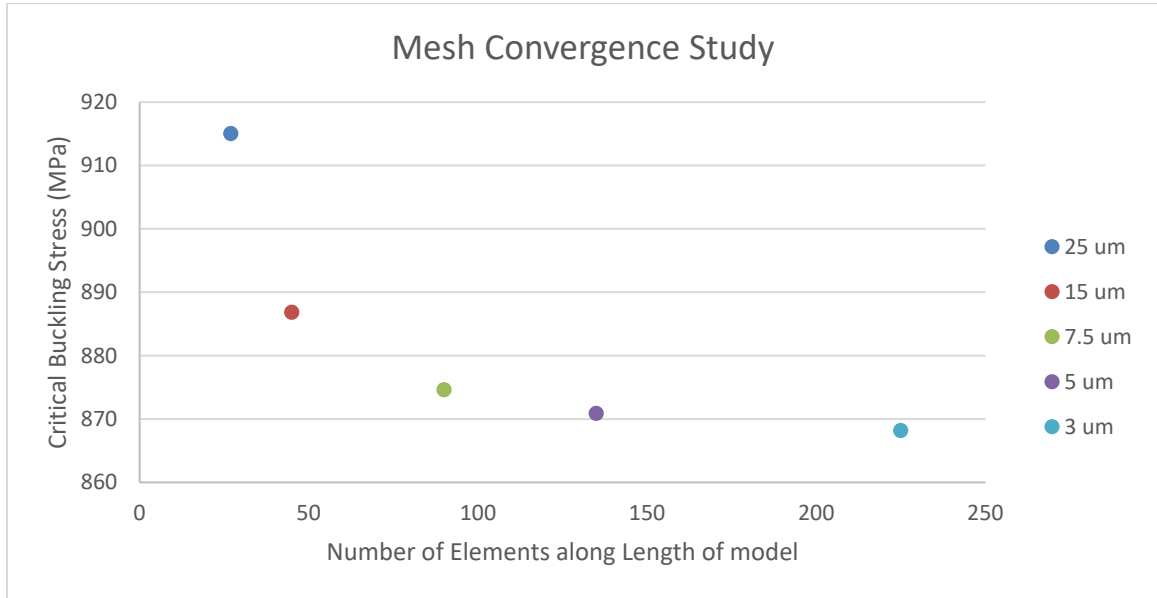
Figure 33: Mesh convergence study results where points represent lateral lengths of individual elements that make up mesh of model

<div align="center">Material Model</div>

Carbon fiber and Hexion Epikote/Epicure Epoxy properties were used to simulate

the fiber and matrix materials, respectively, with the elastic values used shown in Table 1

[51]. The fiber is assumed to be linear elastic and isotropic. Since fiber kinking by its

definition is an inelastic phenomenon of the matrix, the matrix must be modeled as an

elasto-plastic material.

Table 1: Elastic properties of fiber and matrix material used [51].

Fiber Young's Modulus, E_f (GPa)	Fiber Poisson's Ratio, v_f	Matrix Young's Modulus, E_m (GPa)	Matrix Poisson's Ratio, v_m
228	0.30	3.16	0.347

Plasticity Model Calibration

The inelastic region of the matrix was modeled with a Von Mises Yield Criterion, sometimes referred to as J_2 flow theory. Since in fiber kinking the polymer matrix deforms primarily in shear, the experimental shear stress-strain curve of Hexion Epikote MGS RIMR 135/Epicure MGS RIMH 1366 was used to calibrate the plasticity model in ABAQUS CAE (Figure 34). To accomplish this the shear stress-strain curve was first converted to an equivalent Von Mises stress and strain using the pure shear simplification of the Von Mises Yield Criterion as shown in Equations (28) and (29) respectively.

$$\sigma_{vm} = \sqrt{3}\tau \tag{28}$$

$$\epsilon_{vm} = \frac{\gamma}{\sqrt{3}} \tag{29}$$
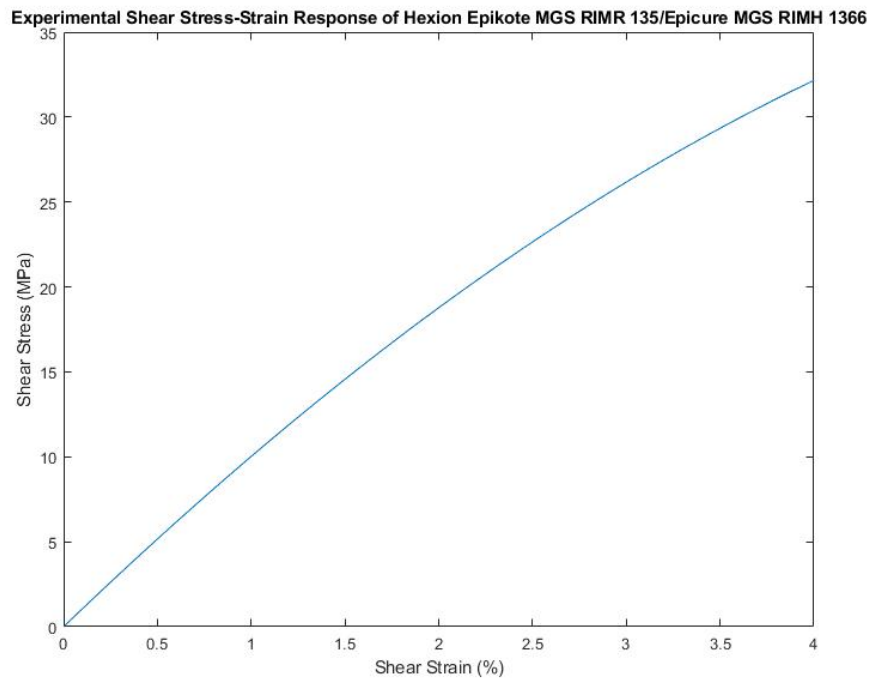
Figure 34: Experimental shear stress-strain curve used to calibrate matrix plasticity model [51].

The resulting equivalent stress-strain curve was then used to calibrate the matrix plasticity model in ABAQUS. Since there is a limit to how far the experimental shear stress-strain curve was tested, the model strains at a constant stress after 4% strain.

Solver and Post-Processing

To solve the compression step of the non-linear RUC model the Modified-Riks algorithm in ABAQUS CAE was used to account for the potential snap-through and snap-back behavior. To solve for the compressive response of the composite as a whole, the macroscopic stress and strain of the RUC must be solved for. Homogenization theory states that the macroscopic stress is equal to the average normal traction at the base of the RUC. To obtain this the sum of the reaction forces in the z-direction of all the nodes on the bottom face were taken and divided by the cross-sectional area of the RUC as shown in Equation (30). The macroscopic strain was computed from a logarithmic formula shown in Equation (31) where δ is the average z-displacement of all nodes on the top face of the model, and L is total length of the model.

$$\bar{\sigma} = \frac{\Sigma F_{nodes}}{Area} \tag{30}$$

$$\bar{\varepsilon} = \ln(1 + \frac{\delta}{L}) \tag{31}$$

Base Model Modifications

To explore the effect that varying volume fraction and multiaxial loading has on the compressive response of a UD FRP composite, modifications were made to the base model described above.

Volume Fraction

The micromechanical method used in this thesis is a first order method. This means absolute size is not accounted for in the solution and only ratios i.e. volume fraction has any affect. To examine the effect that volume fraction has on compressive strength the square matrix dimensions of the RUC are changed while maintaining the absolute size of the fiber cross-section to account for a volume fractions of approximately 24%, 30%, 34%, and 40% as shown below in Figure 35. Models above 40% volume fraction were unable to be analyzed in this study because of the geometric constraint the kidney-shaped fibers provided. The major axis of the kidney shaped fiber was $9\mu m$ in length meaning that to maintain a square RUC model 40% was about the highest volume fraction possible.

$V_f = 24\%$ $V_f = 30\%$ $V_f = 34\%$ $V_f = 40\%$
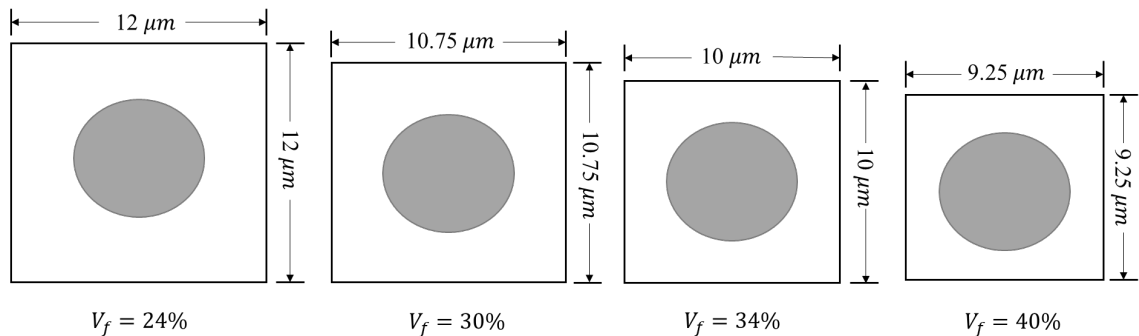
Figure 35: The four RUCs used to represent the volume fractions: 24%, 30%, 34%, 40%.

Applied In-Plane Shear Stress

A common type of multiaxial loading that advanced composite structures experience is in-plane shear stress along with compressive stress. To accurately simulate this type of loading on the model developed in this thesis, the loads were applied in two separate steps in ABAQUS CAE. In the first step the shear stress was applied as a shear displacement on the front face nodes (See point 3 in Figure 27). The shear displacements were calibrated to accurately represent three shear stress levels: 10 MPa, 20 MPa, and 30 MPa. In the second step the compressive stress is applied as an incremental displacement to the front face using the Rik's algorithm.

Assumptions and Limitations

In every model, no matter how complex there are built in assumptions and limitations that will deviate from the true physics of the problem. The models developed in this thesis are no different, while the models used do capture the fundamental physics of the problem there are still various aspects of compression failure in composites that is not accounted for.

1.) **PBC Implications**: the use of PBCs to simulate the bulk composite material as a RUC in fiber kinking implies that the kink band angle β equals 0°. Additionally, it also implies that the kink band propagates instantaneously across the composite specimen. Obviously, this is not what happens in reality. Gutkin et al. [26] tested the effect of this assumption on compressive strength predictions by modeling a 2-D RUC with PBCs applied to its lateral faces and compared it to a 2-D model with 100 fibers explicitly modeled. He found that

the compressive strength does not change between the two models. Since the models used in this thesis make use of PBCs no information can be obtained about the effect that fiber shape could have on the propagation characteristics of fiber kinking.

2.) **Plasticity Model Implications**: Another assumption present in the models of this thesis pertains to the plasticity modeling of the matrix material. A Von Mises Yield Criterion was used to characterize the plastic yielding of the matrix; this is a relatively simple yield criterion and may not capture the full complexity of the yielding behavior of a polymeric material. Some researchers state that a Von Mises criterion neglects the pressure sensitivity that many polymeric materials exhibit. While that may be true for thermoplastic polymer material which does exhibit pressure sensitivity. The matrix that was modeled in this thesis is a thermoset epoxy, which with its high degree of cross-linking, has negligible pressure sensitivity in its yielding behavior. Another drawback of the Von Mises criterion is inability to capture temporal effects in viscoelastic materials i.e. creep. The assumption to disregard creep in this model was deemed acceptable because the sequence of events that characterize fiber kinking occur so quickly that creep effects can be disregarded.

3.) **Fiber-Matrix Bonding**: The fiber and matrix are perfectly bonded in the models used in this study. In reality, fiber matrix debonding can and does occur. By assuming a perfectly bonded fiber-matrix interface the models used have

the potential to overpredict the compressive strength if the interfacial shear stresses become large enough where debonding could realistically occur.

4.) **Fiber Failure**: The last stage of fiber kinking when final failure occurs is often characterized by a fracturing of the fibers when the bending stresses reach the fiber strength. In the models used in this study the fibers are not allowed to fracture. However, fiber fracture often occurs much later than the peak macroscopic stress after the composite has lost lateral stability. This means that even though the model cannot capture fiber failure it should not have an effect on the peak stress response of the composite.

RESULTS

In the previous section, a numerical base model was developed to predict the compressive response of a UD CFRP composite. In this section, results from different analyses conducted with the numerical model is shown and discussed. First, a validation of PBCs for compressive strength prediction was done with a linear elastic modification of the base model. Second, the various stages of fiber kinking that was captured by the numerical model is discussed. Finally, the effect of fiber misalignment, volume fraction, and multiaxial loading has on UD CFRP compressive failure is explored.

Periodic Boundary Condition Verification

As discussed earlier in the Theory section, Rosen and Dow[21] were the first to come up with an analytical prediction of composite compressive strength. Rosen and Dow's conclusion can be interpreted as composite compressive strength in micro-buckling is equal to composite in-plane shear modulus as shown in Equation (9). To verify the use of PBC on a 3-D RUC to simulate fiber kinking, a linear elastic circular RUC model was developed with all of Rosen's assumptions built-in. An eigenvalue buckling analysis was then performed in ABAQUS with 3 different values for the fiber young's modulus to determine a range of linear elastic buckling strengths predicted by the FE model. The FE model strength values were then compared against a simple closed form analytical solution for composite in-plane shear modulus. The analytical solution used for in-plane shear modulus was the Cylindrical Assemblage Model (CAM) given in Equation (32).

$$G_{12} = G_m \left[\frac{(1 + V_f) + \frac{(1 - V_f)G_m}{G_f}}{(1 - V_f) + \frac{(1 + V_f)G_m}{G_f}} \right] \tag{32}$$

The FE model was in good agreement with the analytical predictions as shown in Table 2. The difference between the FE model and analytical expression decreased with increasing fiber modulus. This is because the assumption of a high fiber modulus to matrix modulus ratio becomes more accurate. To be clear this is an analytical verification of PBCs in the context of fiber kinking and not as robust as a model validation via experimental testing.

Table 2: Comparison of numerical vs. analytical theoretical compressive strengths for different fiber property inputs.

Fiber Young's Modulus (GPa)	FE Predicted Strength (MPa)	Analytical Predicted Strength (MPa)	Difference between FE and Analytical Values (%)
128	2500	2400	4.2
228	2468	2438	1.2
328	2458	2454	0.2

Equation (32) requires the fibers shear modulus to calculate G_{12}, however Table 2 gives the fibers Young's modulus. This is because ABAQUS CAE accepts only the fibers Young's modulus and Poisson's ratio as inputs for an isotropic, linear elastic material and then calculates the fiber shear modulus using Equation (33).

$$G_f = \frac{E}{3(1 - 2v)} \tag{33}$$

Sequence of Events in Fiber Kinking

The sequence of events that characterize fiber kinking are shown below in Figures 35- 44. Five distinct points are identified on the fiber kinking stress-strain response shown in Figure 35. The plastic shear strain of the matrix is shown at the selected five points and presented along with the point along the predicted stress-strain response that the event is occurring. The circular fiber RUC model at 1° misalignment angle was used to show the events involved with fiber kinking.
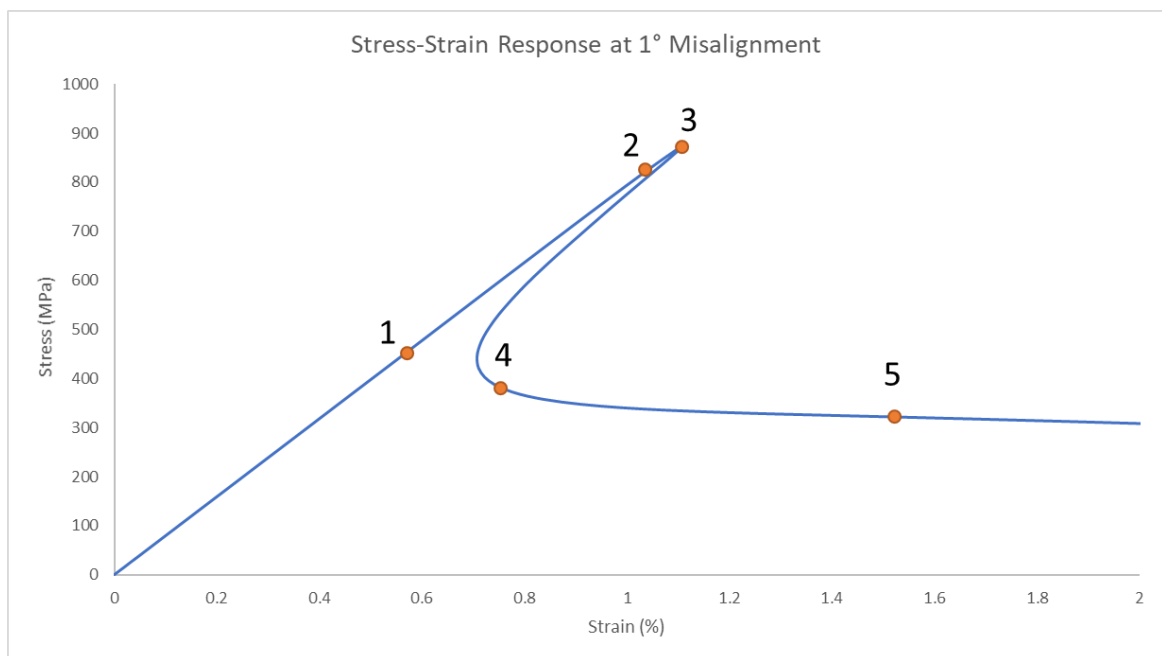
Figure 36: Stress-strain response graph of circular fiber RUC model with 1° misalignment with five regions of fiber kinking shown

The five distinct points are:

1. Linear elastic response of composite specimen.

2. Initiation of plastic strain in matrix.

3. Peak stress reached in composite.

4. Kink band formation.

5. Kink band growth.

The linear elastic region of the initial loading step is shown in Figure 36 and as point 1 in Figure 35. In the first point the polymer matrix has not yielded and therefore no plastic shear strain is present.
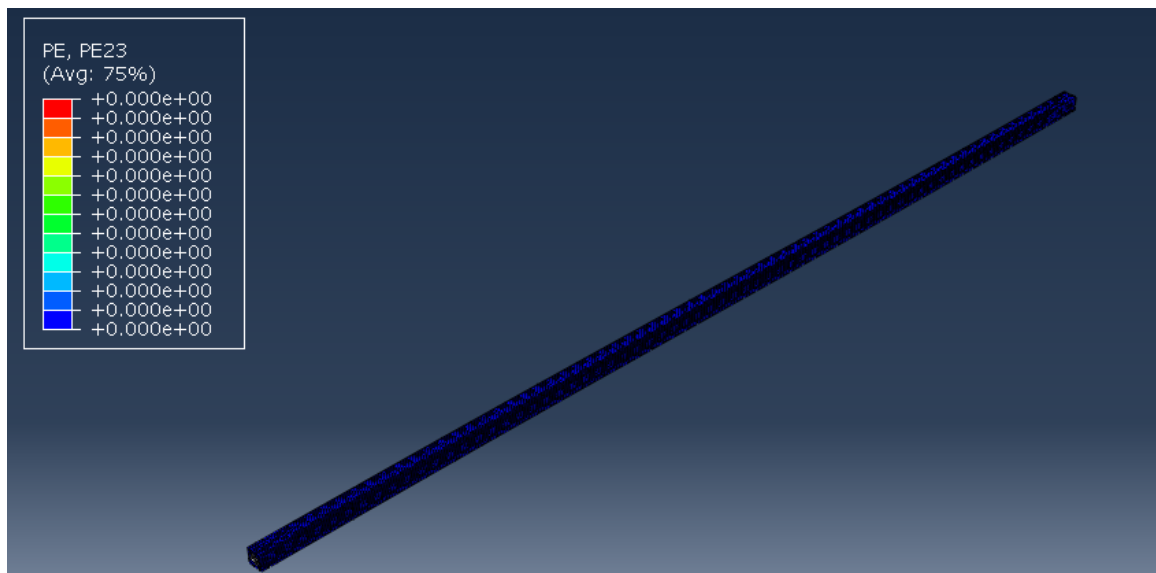
Figure 37: Plastic shear strain map of the matrix in the linear elastic region of the stress-strain response.

The second point shown is characterized by plastic deformation starting to occur within the matrix around the region with the highest misalignment as shown in Figure 38 and Figure 39. When the periodic fibers are closer to one another it creates creating a more severe shear deformation in those areas. This can be seen by the larger shear deformation occurring near the center of the RUC. At this region in the fiber kinking response the stress-strain response starts to become non-linear as shown as point 2 in Figure 35.
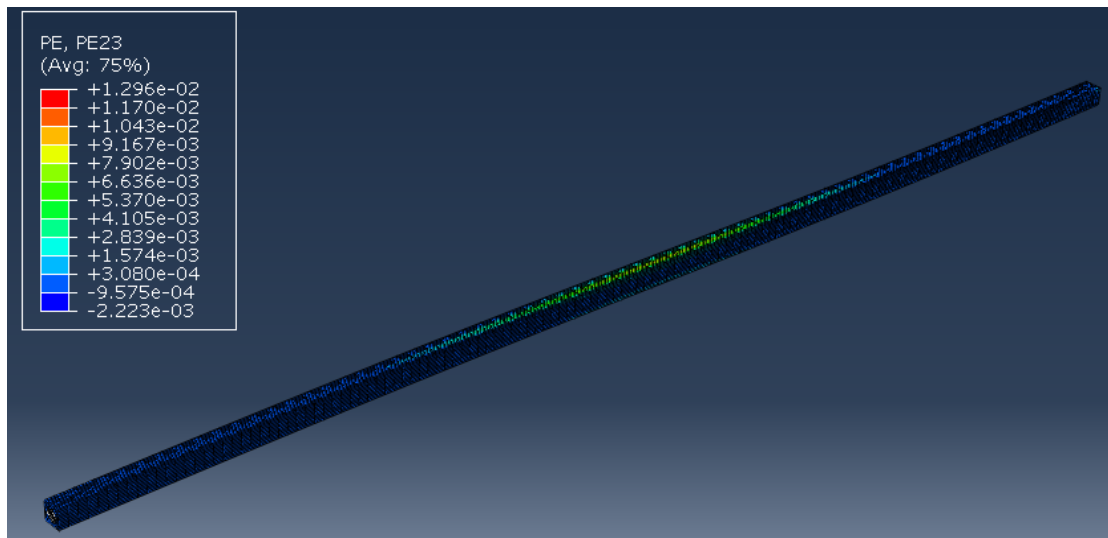
Figure 38: Plastic shear strain map of the matrix when plastic deformation is starting to form in the model.
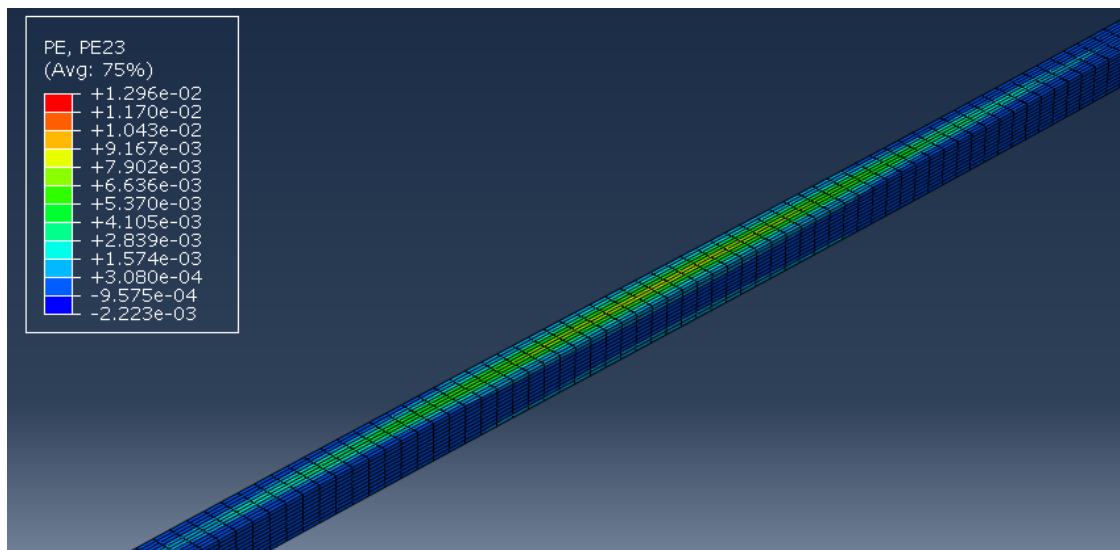
Figure 39: Close up view of plastic shear deformation around area of largest misalignment at point 2.

The third point in fiber kinking is when peak stress is reached as shown as point 3 in Figure 35. The local yielding of the matrix has continued from point 2 (Figure 35) and has become wide enough to promote large rotation in the fiber. Plastic shear deformation

continues to increase around the midsection of the model following the same pattern as in

point 2 (Figure 39 and Figure 40).
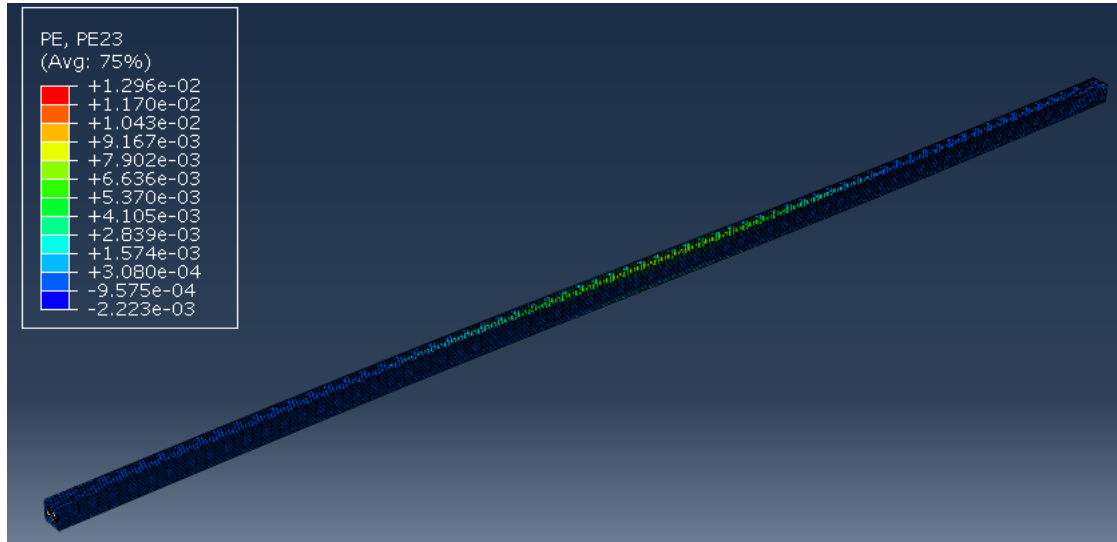
Figure 40: Plastic shear strain map of the matrix at peak stress of the model, right before loss of lateral stability.
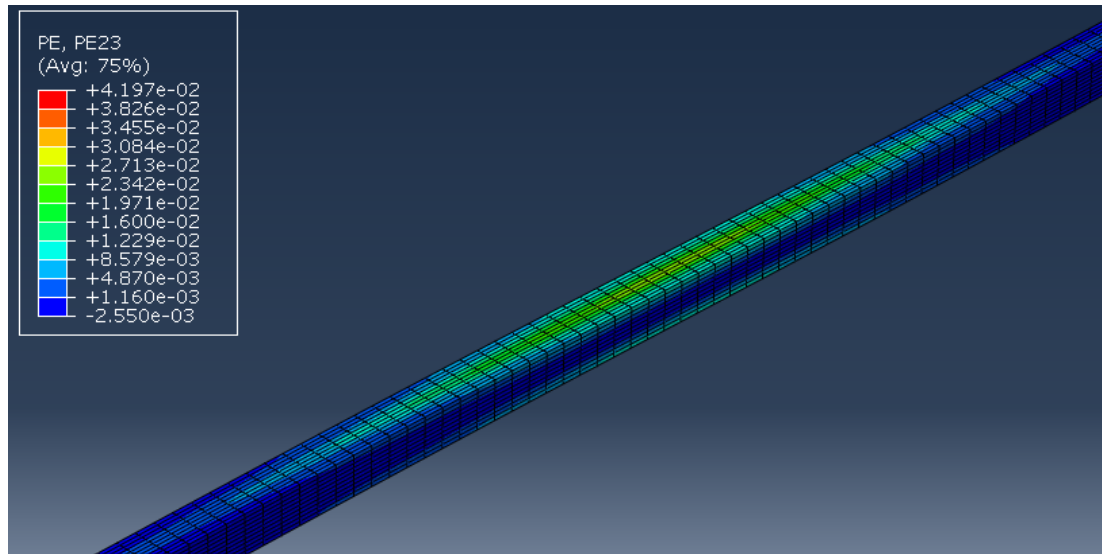
Figure 41: Close-up view of plastic shear deformation around area of largest misalignment at point 3.

In the fourth point of fiber kinking, point 4 in Figure 35, the RUC model has lost

lateral stability and the kink band has formed as seen in Figure 41 and Figure 42. Kink

band formation is accompanied by a sudden drop in load carry capacity of the composite. As discussed earlier the PBCs make it so the transverse propagation of the kink band is instantaneous across the entire composite and so the model begins to immediately broaden in the fiber direction. The plastic shear deformation becomes most severe around the boundaries of the kin band at the point of largest bending stresses.
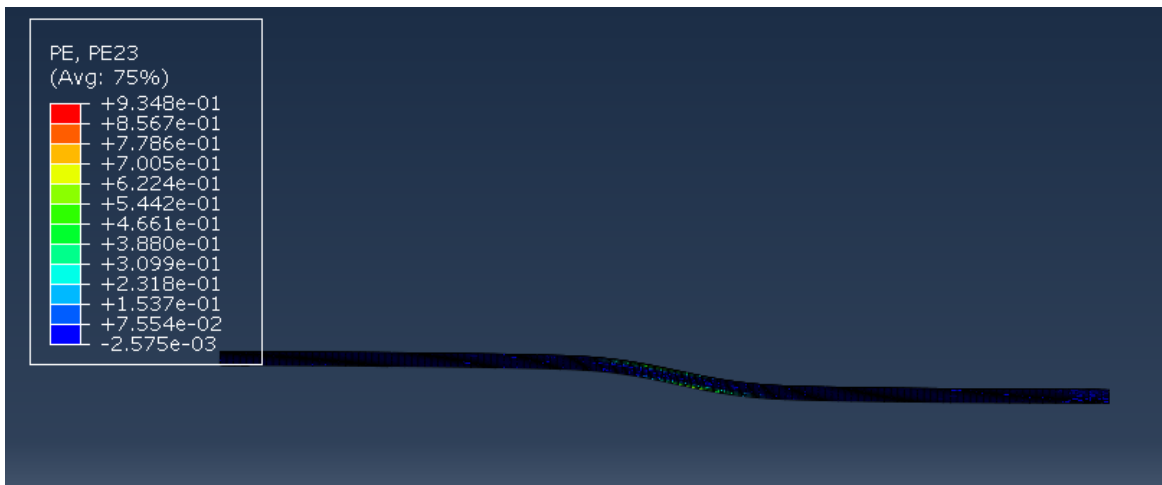
Figure 42: Side view of the RUC model at the moment when the kink-band has fully developed.
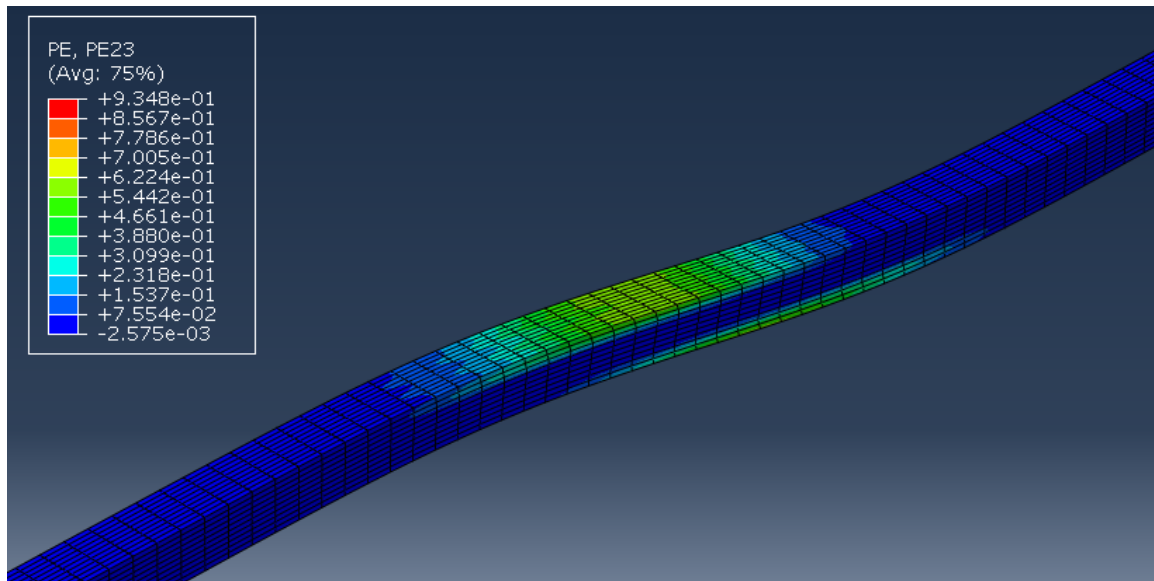
Figure 43: Close-up view of the fully formed kink band in the RUC model.

The point region of kink band formation shows band broadening of the kink band along the fiber direction. The kink band grows at a semi-constant residual stress level and the fiber rotation continues to increase. The sequence of events discussed above has also been observed experimentally with a UD CFRP laminate [30].
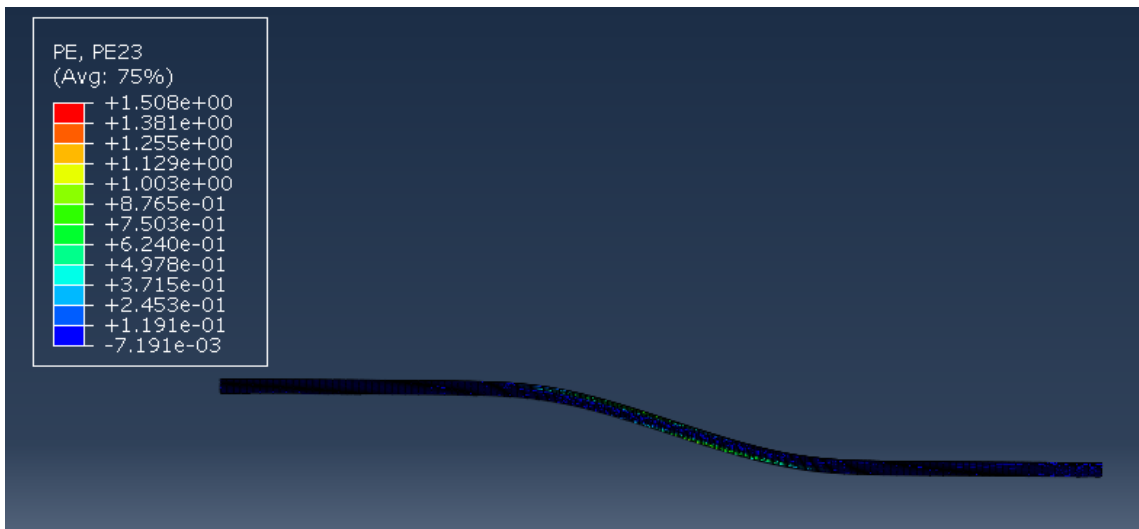
Figure 44: Side view of the growing kink band in the RUC model.
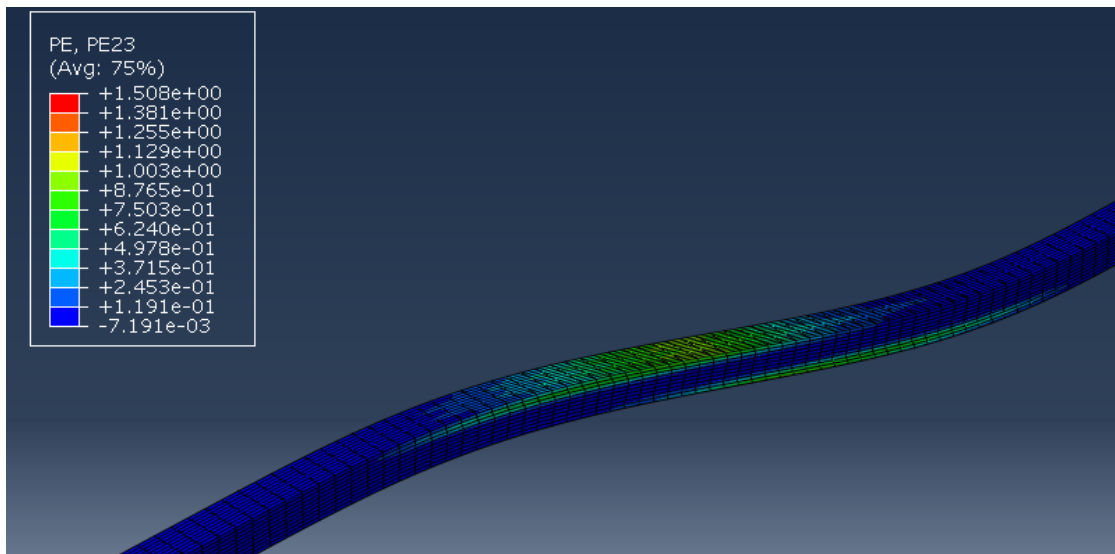
Figure 45: Close up view of the broadening kink band in region five.

Effect of Increasing Fiber Misalignment

Nonlinear buckling analysis was performed for four different fiber shape-orientation combinations: circular, 0° kidney, 45° kidney, and 90° kidney. Each shape-orientation combination was analyzed at five different initial fiber misalignment angles: 1°, 2°, 3°, 4°, and 5°. The stress was calculated in MPa and the strain was calculated as percent strain. The global stress-strain responses of the models at the different misalignment angles can be seen in Figures 45- 48.
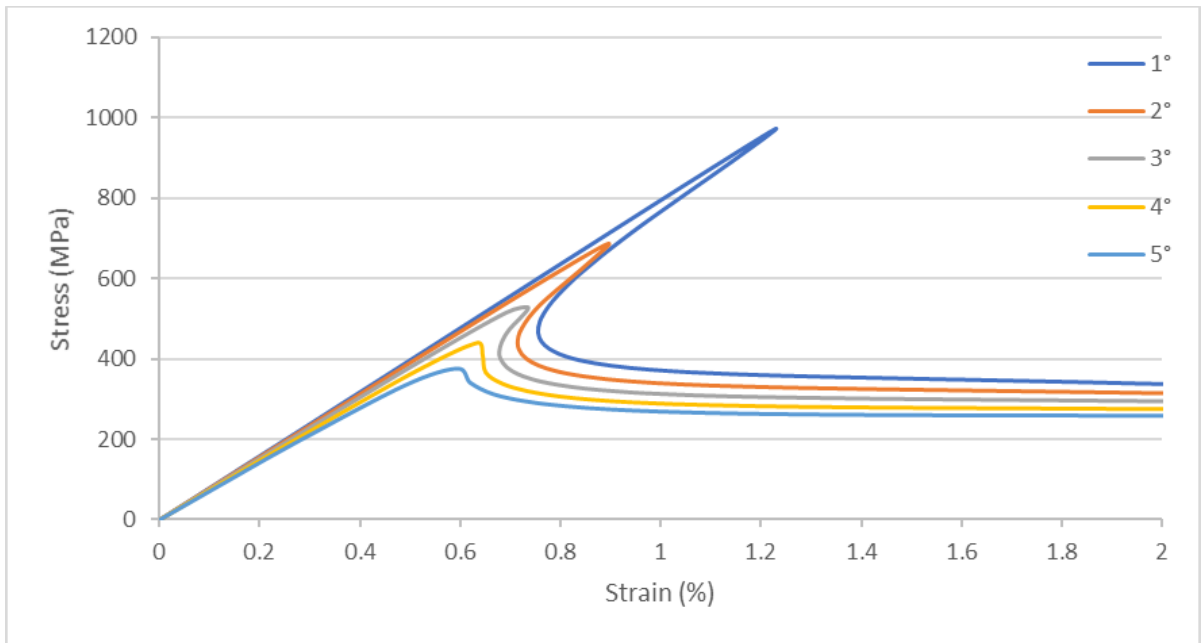
Figure 46: Stress-strain response of fiber kinking of a circular fiber RUC at different initial misalignment angles.
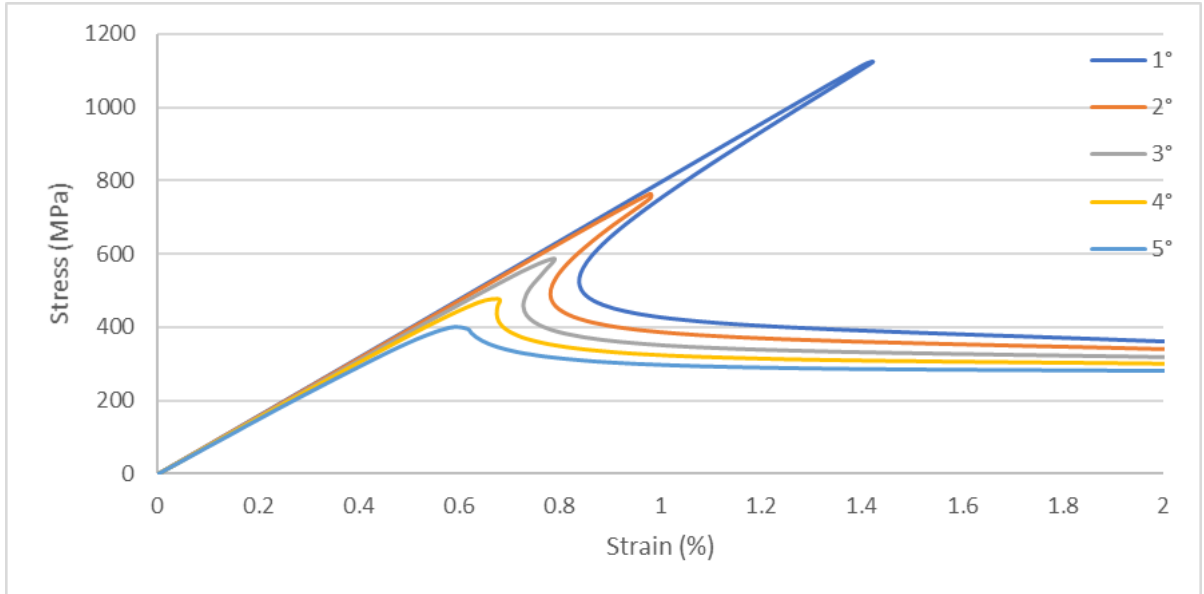
Figure 47: Stress-strain response of fiber kinking of 0° kidney fiber RUC at different initial misalignment angles.
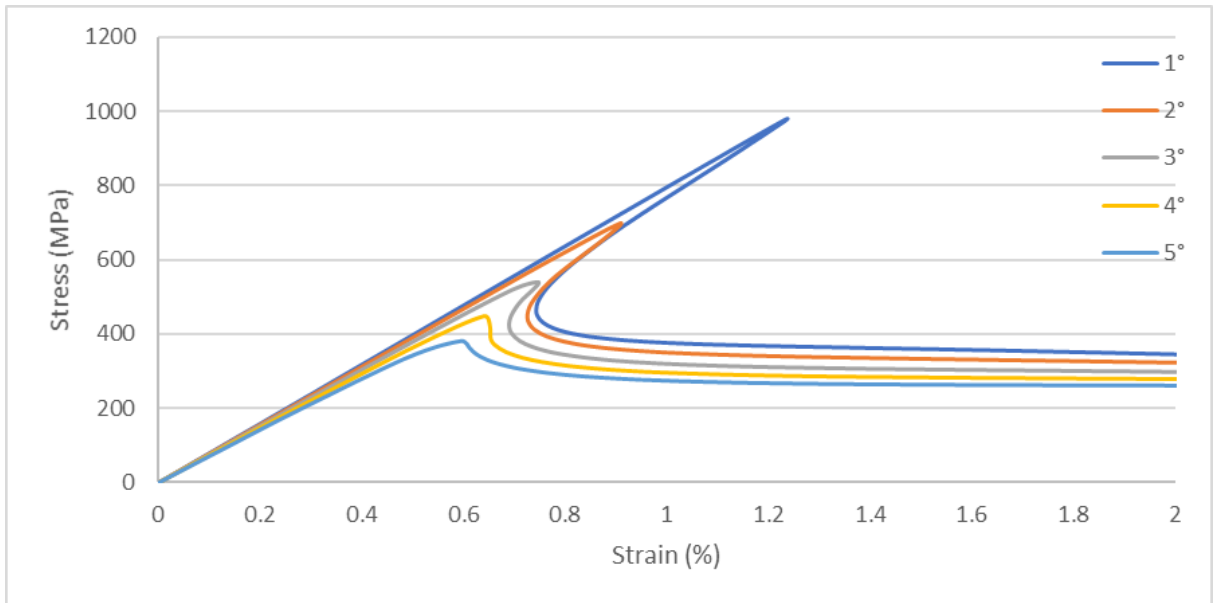
Figure 48: Stress-strain response of fiber kinking of 45° kidney fiber RUC at different initial misalignment angles.
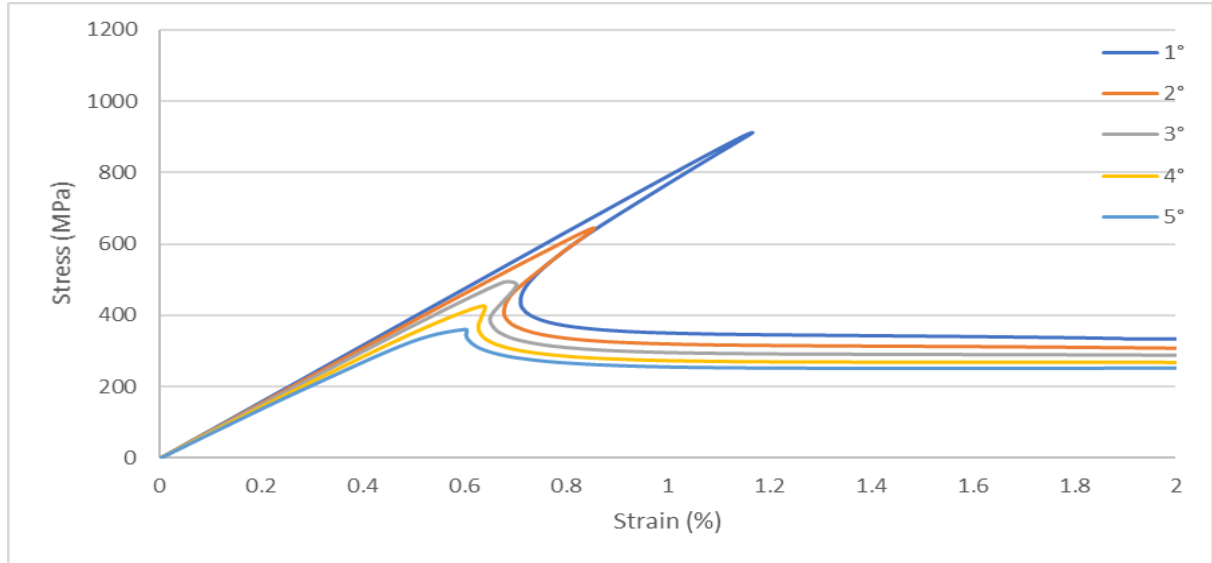
Figure 49: Stress-strain response of fiber kinking of 90° kidney fiber RUC at different initial misalignment angles.

All fiber configurations show a significant reduction in compressive strength with increasing fiber misalignment with an average reduction between 1° and 5° misalignment of 62%. The strains at maximum stress were also significantly reduced at increasing fiber misalignment with an average reduction in failure strain of 52% between 1° and 5° misalignment. The compressive stress-strain response of all fiber configurations showed the same general trends with increasing fiber misalignment. As the misalignment became more severe, the difference in stress between peak stress and residual stress lowered. Also, with increasing misalignment there was larger nonlinearity in the stress-strain response prior to peak stress.

Figure 49 illustrates the significant differences in maximum stress at low misalignment angles between the 0° kidney, 90° kidney, and circular fiber. This result, however, is not representative of a realistic composite. The principle of superposition was used to better compare the kidney shaped fiber versus the circular fiber by averaging the

results of the 3 kidney fiber orientations to represent a composite structure with an even distribution of the different kidney fiber orientations. There is a small increase in compressive strength for the orientation-averaged kidney fiber of 4% in comparison to the circular fiber at 1° fiber misalignment. As shown in Figure 49 the strength results quickly converge at larger misalignments. Even at 1° misalignment, however, a 4% increase in strength is well within the error of the model presented and there appears to be no effective difference between the two fiber shapes.

The results shown in Figure 49 show a high-imperfection sensitivity for maximum strength at low misalignment angles that quickly becomes less sensitive at larger misalignment angles. For example, there was a 30% reduction in maximum strength for the circular fiber RUC between 1° and 2° misalignment. The reduction in maximum strength between 4° and 5° misalignment for the circular fiber RUC model was 17%. This is indicative of a quick transition from a primarily fiber dominated response at low misalignment angles to a matrix shear dominated response at larger misalignment angles.
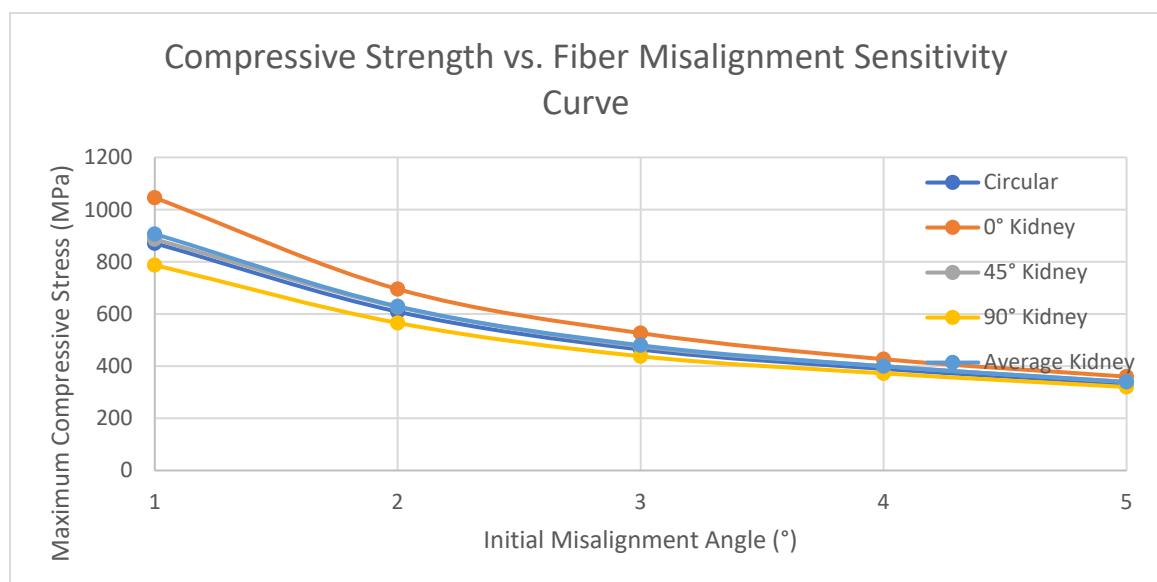
Figure 50: Maximum compressive stress sensitivity curves of the different fiber types.

Effect of Varying Volume Fraction

The mechanical properties of a composite are largely dependent on the fiber volume fraction. The tensile properties in the fiber direction of a UD FRP composite material tend to increase linearly with an increase in fiber volume fraction because tensile properties tend to be fiber-dominated. Since compressive strength is a matrix-dominated property the relationship between volume fraction and composite compressive strength is complex. In this study the four base model RUCs with the different fiber configurations, outlined previously, were modified to represent four fiber volume fractions: 24%, 30%, 34%, and 40%. The models with the different volume fractions were then modeled at five different fiber misalignment angles 1°, 2°, 3°, 4°, and 5°. Misalignment angles were varied to investigate the relationships between fiber configuration, volume fraction, fiber defect severity, and compressive strength. The principle of superposition was applied, and the three kidney fiber orientation results were averaged out to a single orientation-averaged kidney fiber result to have a more accurate comparison of the kidney fiber geometry to the circular fiber geometry.

Figure 50 shows a surface plot of the compressive strength of a composite and how it is affected by a combination of fiber misalignment and varying volume fraction. The translucent surface represents the orientation-averaged kidney fiber RUC model while the opaque surface represents the circular fiber model. Both the averaged kidney fiber model and circular model exhibit the same trends with the averaged kidney fiber having a slightly higher compressive strength at low fiber misalignment angles and higher volume fractions, the strengths quickly converge at lower volume fractions and higher misalignment angles.

However, even at the highest volume fraction of 40% and lowest misalignment angle of 1° the averaged kidney fiber model is only 4.6% stronger than the circular fiber, well within the error contained in the assumptions made in these models.

As can be seen in Figure 50, composite compressive strength has decreasing sensitivity to fiber misalignment angle as the misalignment angle becomes larger. This trend of decreasing sensitivity to fiber misalignment remains the same across all volume fractions. Contrasting the decaying sensitivity of compressive strength to increasing fiber misalignment, the compressive strength linearly increases as the volume fraction increases, this trend also remains the same as fiber misalignment angle increases.
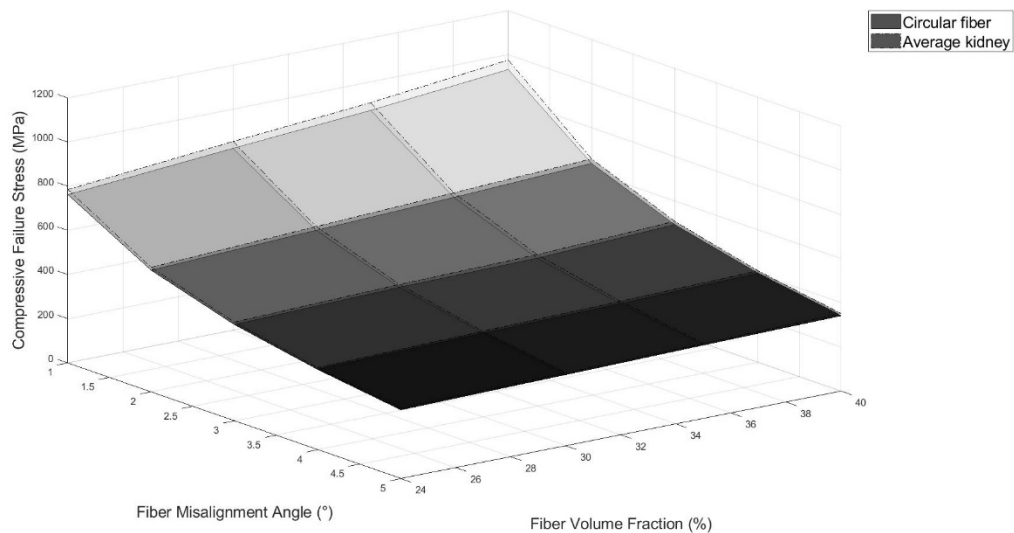
Figure 51: Surface plot of fiber misalignment angle vs. fiber volume fraction vs. compressive strength.

Table 3: Circular fiber RUC compressive strength values at varying misalignment angles and volume factions.

Compressive Strength (MPa)				
	Volume Fraction			
Misalignment Angle	24%	30%	34%	40%
1°	761	823	871	932
2°	551	583	608	638
3°	436	457	464	492
4°	364	379	389	403
5°	312	323	333	342

Table 4: Orientation-Averaged Kidney fiber RUC compressive strength values at varying misalignment angles and volume factions.

Compressive Strength (MPa)				
	Volume Fraction			
Misalignment Angle	24%	30%	34%	40%
1°	785	854	906	975
2°	526	600	629	659
3°	446	469	480	506
4°	372	388	400	414
5°	319	331	340	352

Since the goal of this study is not to accurately model all aspects of composite compressive strength but instead to illustrate general trends and the overall effect different factors have on compressive strength. The percent reduction in strength between the smallest fiber angle defect and largest fiber angle defect at different fiber volume fractions were investigated. The initial fiber misalignment angle was shown to have a strong adverse effect on the compressive strength at all volume fractions as can be seen in Table 3 and Table 4. The circular fiber RUC has an average reduction in strength of 61.2% across all volume fractions when increasing the fiber misalignment angle from 1° to 5°. The strength reduction at increasingly larger volume fractions becomes greater although this effect is minimal. The averaged kidney fiber model showed very similar results with an average

reduction of strength across all volume fractions of 61.8% when increasing fiber misalignment from 1° to 5°. The averaged kidney fiber model also showed insensitivity to fiber volume fraction in terms of strength reduction from increasing fiber misalignment similar to the circular fiber model.

Decreasing the fiber volume fraction by 16% has a relatively small effect on compressive strength reduction of the composite for either the circular fiber or averaged kidney fiber model compared to increasing fiber misalignment (Table 3 and Table 4). The largest strength reduction from decreasing fiber volume fraction occurs at the lower fiber misalignment angles, with a strength reduction of 18.3% for the circular fiber and a strength reduction of 19.5% for the averaged kidney fiber at 1° misalignment. The sensitivity to decreasing fiber volume fraction for both fiber models is significantly decreased at larger fiber misalignment angles with a strength reduction of 8.8% for the circular fiber model and a strength reduction of 9.4% for the averaged kidney model at 5° misalignment.

Figure 51 shows a surface plot of the relationship between compressive failure strain, fiber misalignment angle, and fiber volume fraction with the translucent surface again representing the orientation-averaged kidney fiber RUC model and the opaque surface representing the circular fiber RUC model. Interestingly, the compressive failure strain exhibits an opposite trend to the compressive strength at varying fiber volume fractions with an increase in compressive failure strain at lower volume fractions. However, the effect of fiber misalignment is still the same with a significant decrease in failure strain at larger misalignment angles and a decreasing sensitivity to increasing misalignment angles at larger misalignment angles.

Much like compressive strength there is very little difference between the failure strains of the averaged kidney fiber model and the circular fiber model. The largest difference again is seen at low misalignment angles and higher volume fractions with the averaged kidney fiber model having a 4.2% increase in strength over the circular fiber model at 1° misalignment and 40% fiber volume fraction.
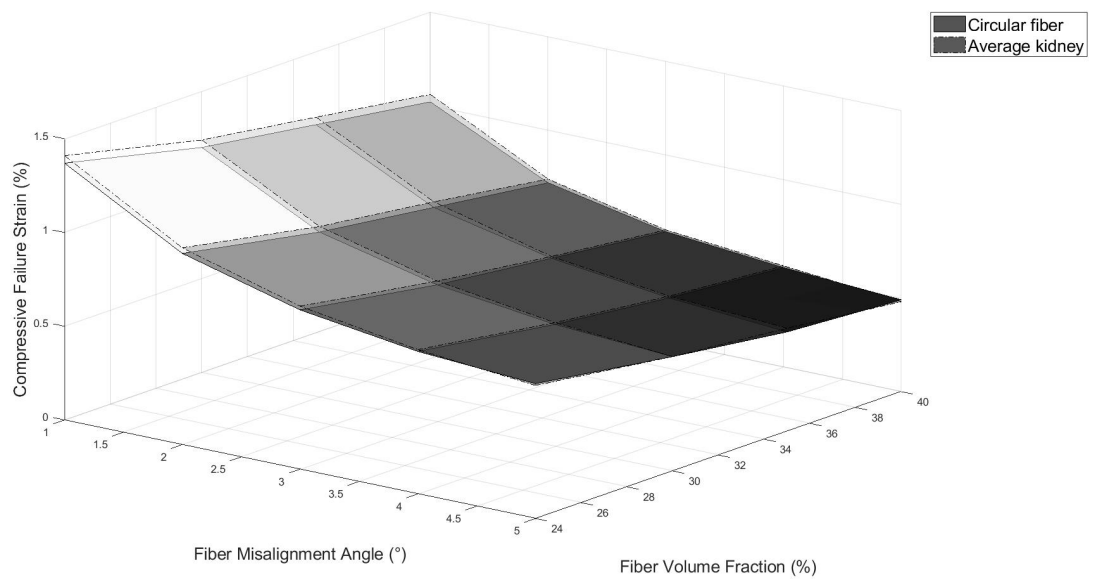
Figure 52: Surface plot of fiber misalignment angle vs. fiber volume fraction vs. compressive failure strain.

Table 5: Circular fiber RUC compressive failure strain values at varying misalignment angles and volume factions.

Compressive Failure Strain (%)				
	Volume Fraction			
Misalignment Angle	24%	30%	34%	40%
1°	1.37	1.20	1.11	1.02
2°	1.02	0.88	0.80	0.72
3°	0.85	0.73	0.66	0.59
4°	0.76	0.65	0.58	0.53
5°	0.72	0.59	0.53	0.48

Table 6: Orientation-averaged kidney fiber RUC compressive failure strain values at varying misalignment angles and volume factions.

Compressive Failure Strain (%)				
	Volume Fraction			
Misalignment Angle	24%	30%	34%	40%
1°	1.41	1.24	1.15	1.06
2°	1.05	0.91	0.83	0.74
3°	0.87	0.75	0.67	0.60
4°	0.77	0.66	0.59	0.54
5°	0.71	0.61	0.55	0.48

Like the compressive strength the percent reduction in failure strain between the smallest fiber angle defect and largest fiber angle defect at different fiber volume fractions was examined. The average percent reduction in strength across all fiber volume fractions simulated was 51.0% for the circular fiber model and 51.9% for the average kidney fiber model. Both fiber models showed relative insensitivity in terms of changes in the percent failure strain reduction across varying volume fractions.

Unlike the compressive strength reduction, which was insensitive to changes in fiber volume fraction, the compressive failure strain showed large gains when decreasing the volume fraction by 16%. The failure strain increased an average of 43.5% and 42.2% for the circular and averaged kidney fiber models respectively across all fiber misalignment angles simulated when the volume fraction was decreased from 40% to 24% (Table 5 and Table 6). The failure strain gains due to decreasing volume fraction show a general trend in increasing difference in failure strain between the lowest and highest volume fractions at larger fiber misalignment angles.

Effect of Shear Loading on Compression Strength

The previous sections of this thesis have examined the response of a UD FRP composite to uniaxial loading. It is a three-dimensional world, however, and all large-scale composite structures will at some point be subjected to multiaxial loading. To determine the effect multiaxial loading has on compressive strength of a UD FRP composite the combination of in-plane shear loading with compressive loading was examined along with variable fiber defect geometry. The four base fiber RUC models outlined previously were used. The principle of superposition was once again used for the different orientations of kidney fiber RUCs to average their results out to an orientation-averaged kidney fiber to compare to the circular fiber. Shear stresses were applied to the models at four magnitudes: 0 MPa, 10 MPa, 20 MPa, and 30 MPa. Five different fiber misalignment angles were then modeled at each shear stress magnitude: 1°, 2°, 3°, 4°, and 5°.

Figure 52 shows a surface plot of the interaction between composite compression strength, fiber misalignment angle, and applied in-plane shear stress. The translucent surface represents the orientation-averaged kidney fiber RUC model and the opaque surface represents the circular fiber RUC. The orientation-averaged kidney fiber model showed slightly improved compressive strength characteristics than the circular fiber model at low misalignment angles and high shear stress values. The averaged kidney model greatest increase in strength over the circular fiber model was 7.1% at 1° fiber misalignment and 30 MPa applied in-plane shear stress. The strength values between the averaged kidney fiber model and circular model quickly converge at larger fiber misalignment angles.

The relationship between compressive strength and fiber misalignment angle continues to show decaying sensitivity as fiber misalignment angle becomes larger as seen in previous results in this thesis (Figure 52). The relationship between compressive strength and applied in-plane shear stress is linear with a similar drop in compressive strength from 0 MPa shear stress to 10 MPa shear stress, as there would be between 10 MPa and 20 MPa (Figure 52).

Figure 53: Surface plot of fiber misalignment angle vs. applied in-plane shear stress vs. compressive failure strength.

Table 7: Circular fiber RUC compressive strength values at varying misalignment angles and applied in-plane shear stress.

Compressive Strength (MPa)				
	Applied In-plane Shear Stress			
Misalignment Angle	0 MPa	10 MPa	20 MPa	30 MPa
1°	871	620	393	199
2°	608	444	292	155
3°	464	351	236	128
4°	389	289	199	110
5°	333	251	172	96

Table 8: Orientation-averaged kidney fiber RUC compressive strength values at varying misalignment angles and applied in-plane shear stress.

Compressive Strength (MPa)			
	Applied In-plane Shear Stress		
Misalignment Angle	0 MPa	10 MPa	20 MPa	30 MPa
1°	906	649	416	213
2°	566	463	308	164
3°	480	363	246	134
4°	400	302	206	114
5°	340	257	178	100

The relative change in strength reduction between the smallest fiber angle defect and largest fiber angle defect at different applied in-plane shear stress is next examined in this section. Both the orientation-averaged kidney fiber model and circular fiber model show similar reductions in compressive strength from 1° misalignment to 5° misalignment at varying in-plane shear stress values (Table 7 and Table 8). Across all shear stress levels, the circular fiber model and orientation-averaged kidney fiber model showed an average reduction in strength of 57.3% and 58.3%, respectively. From lowest to the largest fiber misalignment angle the reduction in strength of both the circular fiber and averaged kidney fiber models was insensitive to increasing in-plane shear stress with the strength reduction only decreasing about 10% from 0 MPa to 30 MPa shear stress.

In-plane shear stress had a detrimental effect on the composite's compressive strength with an average compressive strength reduction of 73.4% and 72.9% for circular and averaged kidney fiber models respectively for a change in in-plane shear stress from 0 MPa to 30 MPa. Increasing the fiber misalignment angle did not have a large effect on the strength reduction due to in-plane shear stress, with the relative strength reduction remaining mostly constant across all shear stress values.

Figure 53 shows a surface plot of the interaction between composite compressive failure strain, fiber misalignment angle, and applied in-plane shear stress. The translucent surface again represents the orientation-averaged kidney fiber RUC model and the opaque surface represents the circular fiber RUC. The compressive failure strain surface plot (Figure 53) shows the same general trends between fiber misalignment and applied in-plane shear stress as the above compression strength plot. There is a negative linear relationship between increasing in-plane shear stress and compressive failure strain and a decaying sensitivity of compressive failure strain to increasing fiber misalignment angle.

There are nominal differences between the compressive failure strains of the circular and averaged kidney models. Any difference between the circular and averaged kidney fiber model's failure strains are well within the error of the models and no conclusions can be reliably drawn from the results.
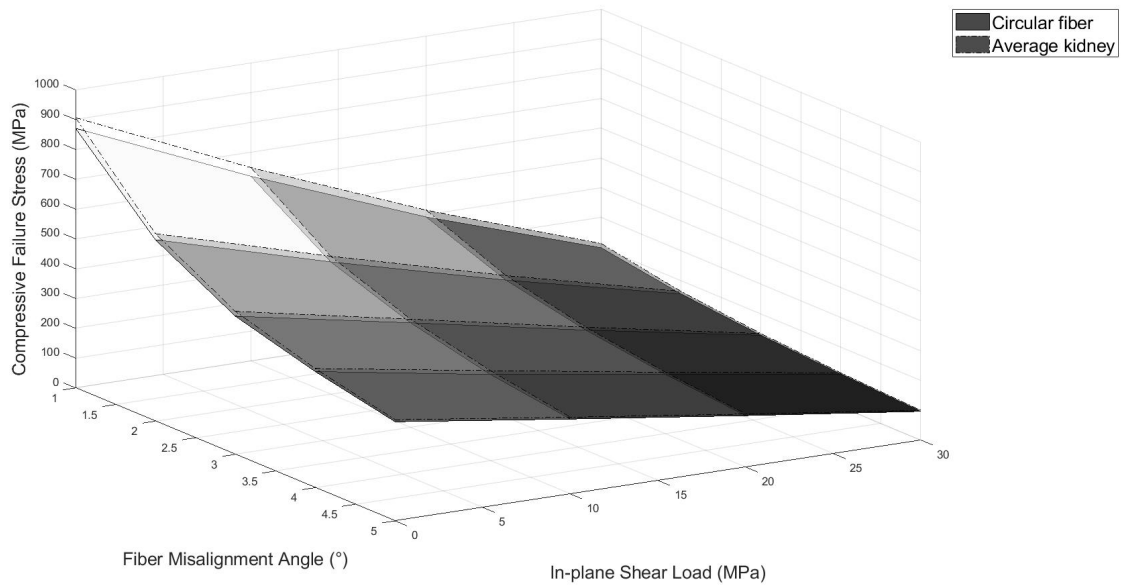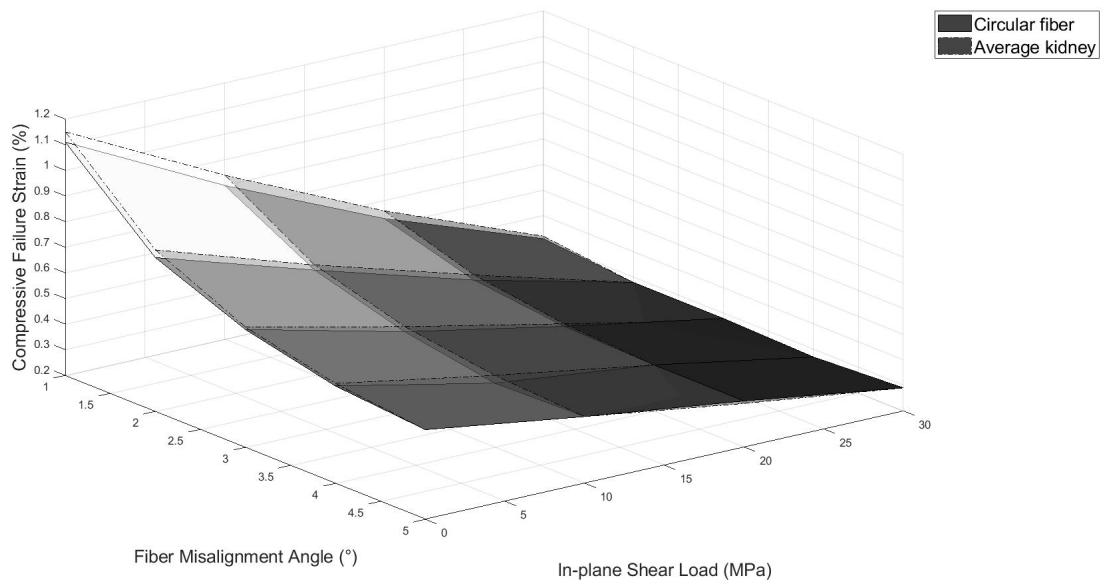

Figure 54: Surface plot of fiber misalignment angle vs. applied in-plane shear stress vs. compressive failure strain.

Table 9: Circular fiber RUC compressive failure strain values at varying misalignment angles and applied in-plane shear stress.

Compressive Failure Strain (%)			
	Applied In-plane Shear Stress		
Misalignment Angle	0 MPa	10 MPa	20 MPa	30 MPa
1°	1.11	0.80	0.53	0.31
2°	0.80	0.61	0.43	0.28
3°	0.66	0.51	0.39	0.28
4°	0.58	0.47	0.38	0.28
5°	0.55	0.46	0.38	0.28

Table 10: Orientation-averaged kidney fiber RUC compressive failure strain values at varying misalignment angles and applied in-plane shear stress.

Compressive Failure Strain (%)			
	Applied In-plane Shear Stress		
Misalignment Angle	0 MPa	10 MPa	20 MPa	30 MPa
1°	1.15	0.84	0.56	0.32
2°	0.83	0.63	0.45	0.28
3°	0.67	0.53	0.40	0.27
4°	0.59	0.48	0.38	0.27
5°	0.55	0.46	0.37	0.27

The relative change in failure strain reduction between the smallest fiber angle defect and largest fiber angle defect at different applied in-plane shear stress is examined next in this section. At low applied in-plane shear stress the reduction in compressive failure strain for both circular and averaged kidney fiber (Table 7 and Table 8) is similar to reduction in compressive strength (Table 9 and Table 10) from low fiber misalignment to large fiber misalignment. For example, the failure strain for the circular fiber model was reduced by 50.6% from 1° misalignment to 5° at an in-plane shear stress of 0 MPa. However, as the applied in-plane shear stress increases, the effect that the increased fiber misalignment has on the compressive failure strain is lessened considerably. In comparison,

at an in-plane shear stress of 30 MPa increasing fiber misalignment from 1° to 5° reduces the compressive failure strain by 6.6% for the circular fiber.

In-plane shear stress had a detrimental effect on the composite's compressive failure strain. From 0 MPa to 30 MPa (Table 9 and Table 10), failure strains were reduced by 71.9% and 72.0% for the circular and averaged kidney fiber, respectively. These reductions were similar to the compressive strength reductions in Table 7and Table 8. Unlike the compressive strength, increasing the fiber misalignment angle had a large effect on the failure strain reduction due to in-plane shear stress, with the relative failure strain reduction lowering from 71.9% at 1° misalignment to 46.9% at 5° misalignment for the circular fiber model.

CONCLUSIONS

The primary objective of this thesis was to compare the effect that fiber cross-sectional shape has on the compressive failure response of UD CFRP composites. It was shown that in most cases the global compressive response between the two fiber shape composites were nearly identical. The differences that occur due to the microscopic shape change is 'homogenized' out when converted into a macroscopic response. One consequence of this conclusion is that it validates the assumption to neglect fiber bending effects that many fiber kinking analytical expressions use. One advantage the kidney shaped fiber composite may have over the circular fiber composite is under a multiaxial load state with large in-plane shear stresses, the kidney fiber composite was able to better retain its compressive load resistance.

The results for the PBC validation indicate that PBCs are valid for simulating the compressive failure response of a 3-D UD CFRP composite. The sequence of events in fiber kinking results show that the model developed in this thesis is able to capture the general physics observed throughout the fiber kinking process and not just the peak response.

The results from varying fiber defect geometry indicate a decaying sensitivity of CFRP compressive strength to increasing fiber misalignment angle. This means that there is potential for great improvements in the compressive response of a composite structure if the manufacturing processes tolerances have the potential to be very high (i.e. +/- 1°), such as in pre-impregnated fiber composites, pultrusion, and autoclave processes. However, there is not much to be gained in incremental improvements if the manufacturing method

can only maintain a tolerance within multiple degrees, such as in Vacuum Assisted Resin Transfer Molding processes.

Varying the volume fraction showed a decrease in ultimate compressive strength with a decrease in volume fraction. An unexpected result was the significant increase in compressive failure strain with a decrease in volume fraction. This could be an important design consideration for large scale flexible structures such as some of the concept designs found in the Big Adaptative Rotor (BAR) project report [52]. The increased flexibility of a wind turbine rotor decreases the operational loads experienced by the structure, so strain at failure becomes more important and overall composite compressive strength less so. The results of the volume fraction section suggest that for these types of structures a lower volume fraction composite could offer benefits over the traditional composite design methodology that "a higher volume fraction is better."

Multiaxial loading via a combination of shear loading and compression loading was shown to have a detrimental effect on the compressive strength properties of a UD CFRP composite. The addition of a relatively small shear load can decrease the compressive load carrying capacity of a composite structure by over 50%. Shear stress should be minimized in composite structures that expect to carry large compressive loads i.e. wind blades. This is an issue in modern turbines were the size of the turbine means shear stresses due to gravitational loads begin to become significant.

The results discussed above show trends that must be considered in the design methodology to optimize compressive strength of composite structures. High fiber alignment is critical for compressive strength. Lower fiber volume fraction may have

benefits for highly flexible composite structures. Shear stress should be minimized in design for optimal compressive strength properties. Finally, the fiber cross-sectional shape appears to have a minimal effect on compression strength. Greater gains in compression strength comes from optimizing the in-plane shear modulus of the composite, this is accomplished through improving matrix and fiber-matrix interfacial properties

Future Work

There are many assumptions made in the micromechanical model presented that should be explored further with improvements to the model. As shown by Prabhakar and Waas [40] fiber-matrix debonding can prematurely induce fiber kinking. By assuming a perfectly bonded fiber-matrix interface fiber-matrix debonding was not considered in this study. The effect of different fiber surface areas between the kidney shaped fiber and circular fiber could be explored by adding cohesive zone elements to the micromechanical model developed in this thesis. Fiber fracture was also not considered and should be included to determine if changing fiber shape could lead to premature fiber fracture before fiber kinking. Naya et al. [46] determined that while an RUC is sufficiently accurate at predicting up to and at peak compressive response, it cannot accurately determine the post-peak compressive response of a CFRP composite. To determine how the factors studied in this thesis accurately affect post-peak response of a UD CFRP composite an RVE analysis should be conducted. Finally, research should be done on packing factors and the statistical distribution of kidney fiber orientations inn terms of an RVE analysis to provide a better understanding of the possible benefit and drawbacks that changing fiber cross-sectional shape could have.

REFERENCES CITED

[1]   B. Tyra, "Electric Power Monthly with Data," *U.S. Energy Inf. Adm.*, no. July, pp. 1–772, 2019.

[2]   J. B. Jorgensen, "Adhesive Joints in Wind Blades," 2017.

[3]   C. A. Crawford, "the Path From Functional To Detailed Design of a Coning Rotor Wind Turbine Concept," *Proc. Can. Eng. Educ. Assoc.*, no. March, pp. 0–10, 2011, doi: 10.24908/pceea.v0i0.3768.

[4]   B. Ennis *et al.*, "Optimized Carbon Fiber Composites in Wind Turbine Blade Design," Albuquerque, 2019.

[5]   R. Cook, D. Malkus, M. Plesha, and R. Witt, *Concepts and Applications of Finite Element Analysis*, 4th ed. Wiley, 2002.

[6]   E. J. Barbero, *Introduction to Composite Materials Design*. CRC Press, 2010.

[7]   W. M. Peterson, "Effect of Fiber Diameter on Stress Transfer and Interfacial Damage in Fiber Reinforced Composites," 2011.

[8]   P. S. Veers *et al.*, "Trends in the design, manufacture and evaluation of wind turbine blades," *Wind Energy*, vol. 6, no. 3, pp. 245–259, 2003, doi: 10.1002/we.90.

[9]   R. E. Murray, D. Swan, D. Snowberg, D. Berry, R. Beach, and S. Rooney, "Manufacturing a 9-meter thermoplastic composite wind turbine blade," *32nd Tech. Conf. Am. Soc. Compos. 2017*, vol. 1, no. December, pp. 29–43, 2017, doi: 10.12783/asc2017/15166.

[10]   W. Yu, "An Introduction to Micromechanics," *Appl. Mech. Mater.*, vol. 828, pp. 3–24, 2016.

[11]   K. (University of S. Markov and L. (Politecnico di T. Preziosi, Eds., *Heterogenous Media: Micromechanics Modeling Methods and Simulations*. Birkhauser Basel, 2000.

[12]   M. Heidari-Rarani, K. Bashandeh-Khodaei-Naeini, and S. M. Mirkhalaf, "Micromechanical modeling of the mechanical behavior of unidirectional composites – A comparative study," *J. Reinf. Plast. Compos.*, vol. 37, no. 16, pp. 1051–1071, 2018, doi: 10.1177/0731684418779441.

[13]   J. Aboudi, S. Arnold, and B. Bednarcyk, *Micromechanics of Composite Materials*. 2013.

[14] A. Drago and M. J. Pindera, "Micro-macromechanical analysis of heterogeneous materials: Macroscopically homogeneous vs periodic microstructures," *Compos. Sci. Technol.*, 2007, doi: 10.1016/j.compscitech.2006.02.031.

[15] R. Hill, "Elastic properties of reinforced solids: Some theoretical principles," *J. Mech. Phys. Solids*, 1963, doi: 10.1016/0022-5096(63)90036-X.

[16] S. Li, "Boundary conditions for unit cells from periodic microstructures and their implications," *Compos. Sci. Technol.*, vol. 68, no. 9, pp. 1962–1974, 2008, doi: 10.1016/j.compscitech.2007.03.035.

[17] S. Li and A. Wongsto, "Unit cells for micromechanical analyses of particle-reinforced composites," *Mech. Mater.*, 2004, doi: 10.1016/S0167-6636(03)00062-0.

[18] J. Segurado and J. Llorca, "A numerical approximation to the elastic properties of sphere-reinforced composites," *J. Mech. Phys. Solids*, 2002, doi: 10.1016/S0022-5096(02)00021-2.

[19] K. Terada, M. Hori, T. Kyoya, and N. Kikuchi, "Simulation of the multi-scale convergence in computational homogenization approaches," *Int. J. Solids Struct.*, vol. 37, no. 16, pp. 2285–2311, 2000, doi: 10.1016/S0020-7683(98)00341-2.

[20] A. S. Kaddour and M. J. Hinton, "Input data for test cases used in benchmarking triaxial failure theories of composites," *J. Compos. Mater.*, vol. 46, no. 19–20, pp. 2295–2312, 2012, doi: 10.1177/0021998312449886.

[21] W. Rosen and N. Dow, "Evaluations of Filament-Reinforced Composites for Aerospace Structural Applications," Washington D.C., 1965.

[22] W. A., B. C.D., and K. W.G., "A Mechanical Model for Elastic Fiber Microbuckling," *J. Appl. Mec*, vol. 57, pp. 138–147, 1990.

[23] A. M. Waas and C. R. Schultheisz, "Compressive Failure of Composites, Part II: Experimental Studies."

[24] P. M. Jelf and N. A. Fleck, "Compression Failure Mechanisms in Unidirectional Composites," *J. Compos. Mater.*, vol. 26, no. 18, pp. 2706–2726, 1992, doi: 10.1177/002199839202601804.

[25] R. Gutkin, S. T. Pinho, P. Robinson, and P. T. Curtis, "A finite fracture mechanics formulation to predict fibre kinking and splitting in CFRP under combined longitudinal compression and in-plane shear," *Mech. Mater.*, vol. 43, no. 11, pp.

730–739, Nov. 2011, doi: 10.1016/J.MECHMAT.2011.08.002.

[26] R. Gutkin, S. T. Pinho, P. Robinson, and P. T. Curtis, "Micro-mechanical modelling of shear-driven fibre compressive failure and of fibre kinking for failure envelope generation in CFRP laminates," *Compos. Sci. Technol.*, vol. 70, no. 8, pp. 1214–1222, 2010, doi: 10.1016/j.compscitech.2010.03.009.

[27] S. Pimenta, R. Gutkin, S. T. Pinho, and P. Robinson, "A micromechanical model for kink-band formation: Part I — Experimental study and numerical modelling," *Compos. Sci. Technol.*, vol. 69, no. 7–8, pp. 948–955, 2009, doi: 10.1016/j.compscitech.2009.02.010.

[28] P. Prabhakar and A. M. Waas, "Micromechanical modeling to determine the compressive strength and failure mode interaction of multidirectional laminates," *Compos. Part A Appl. Sci. Manuf.*, vol. 50, pp. 11–21, 2013, doi: 10.1016/j.compositesa.2013.03.006.

[29] C. R. Schultheisz and A. M. Waas, "Compressive Failure of Composites, Part I: Testing and Micromechanical Theories," 1996.

[30] Q. Sun *et al.*, "Experimental and computational analysis of failure mechanisms in unidirectional carbon fiber reinforced polymer laminates under longitudinal compression loading," *Compos. Struct.*, 2018, doi: 10.1016/j.compstruct.2018.06.028.

[31] B. Budiansky and N. A. Fleck, "Compressive Failure of Fibre Composites," *J. Mech. Phys. Solids*, vol. 41, no. 1, pp. 183–211, 1993.

[32] P. Prabhakar and A. M. Waas, "Interaction between kinking and splitting in the compressive failure of unidirectional fiber reinforced laminated composites," *Compos. Struct.*, vol. 98, pp. 85–92, 2013, doi: 10.1016/j.compstruct.2012.11.005.

[33] M. B. Herraez Andrew; Gonzalez, Carlos; Lopes, Claudio, "Modeling Fiber Kinking at the Microscale and Mesoscale," 2018.

[34] A. S. Argon, "Fracture of Composites," *Treatise Mater. Sci. Technol.*, vol. 1, pp. 79–114, 1972, doi: https://doi.org/10.1016/B978-0-12-341801-2.50007-2.

[35] B. Budiansky, "Micromechanics," *Comput. Struct.*, vol. 16, no. 1–4, pp. 3–12, 1983, doi: 10.1016/0045-7949(83)90141-4.

[36] E. J. Barbero, "Prediction of Compression Strength of Unidirectional Polymer Matrix Composites," *J. Compos. Mater.*, vol. 32, no. 5, pp. 483–502, 1998.

[37] S. Kyriakides, E. Arseculeratne, E. J. Perry, and K. M. Liechti, "On the

Compressive Failure of Fiber Reinforced Composites," *Int. J. Solids Struct.*, vol. 32, no. 6–7, pp. 689–738, 1995, doi: 10.1016/0020-7683(94)00157-R.

[38] D. C. Lagoudas and A. M. Saleh, "Compressive Failure due to Kinking of Fibrous Composites," *J. Compos. Mater.*, vol. 27, no. 1, pp. 83–106, 1993, doi: 10.1177/002199839302700106.

[39] S. Pimenta, R. Gutkin, S. T. Pinho, and P. Robinson, "A micromechanical model for kink-band formation: Part II-Analytical modelling," *Compos. Sci. Technol.*, 2009, doi: 10.1016/j.compscitech.2009.02.003.

[40] P. Prabhakar and A. M. Waas, "Interaction between kinking and splitting in the compressive failure of unidirectional fiber reinforced laminated composites," *Compos. Struct.*, 2013, doi: 10.1016/j.compstruct.2012.11.005.

[41] L. Zhou, L. Zhao, F. Liu, and J. Zhang, "A micromechanical model for longitudinal compressive failure in unidirectional fiber reinforced composite," *Results Phys.*, vol. 10, pp. 841–848, 2018, doi: 10.1016/j.rinp.2018.08.003.

[42] S.-Y. Hsu, T. J. Vogler, and S. Kyriakides, "Compressive Strength Predictions for Fiber Composites," *J. Appl. Mech.*, vol. 65, no. 1, pp. 7–16, Mar. 1998, doi: 10.1115/1.2789050.

[43] T. J. Vogler, S. Y. Hsu, and S. Kyriakides, "On the initiation and growth of kink bands in fiber composites. Part II: Analysis," *Int. J. Solids Struct.*, 2001, doi: 10.1016/S0020-7683(00)00175-X.

[44] A. M. Waas and C. S. Yerramalli, "The Effect of Fiber Diameter on the Compressive Strength of Composites - A 3D Finite Element Based Study," 2004.

[45] N. D. Barulich, L. A. Godoy, and E. J. Barbero, "On Micro-Buckling of Unidirectional Fiber-Reinforced Composites by Means of Computational Micromechanics," *Lat. Am. J. Solids Struct.*, vol. 13, no. 16, pp. 3085–3106, 2016, doi: 10.1590/1679-78252867.

[46] F. Naya, M. Herráez, C. S. Lopes, C. González, S. Van der Veen, and F. Pons, "Computational micromechanics of fiber kinking in unidirectional FRP under different environmental conditions," *Compos. Sci. Technol.*, vol. 144, pp. 26–35, 2017, doi: 10.1016/j.compscitech.2017.03.014.

[47] M. Smith, *ABAQUS/Standard User's Manual, Version 6.14*. Providence, RI: Dassault Systèmes Simulia Corp, 2014.

[48] N. Vasios, "Nonlinear Analysis of Structures." p. 38, 2015.

[49] Z. Xu, J. Li, X. Wu, Y. Huang, L. Chen, and G. Zhang, "Effect of kidney-type and circular cross sections on carbon fiber surface and composite interface," *Compos. Part A Appl. Sci. Manuf.*, vol. 39, no. 2, pp. 301–307, 2008, doi: 10.1016/j.compositesa.2007.10.015.

[50] M. Romanowicz, "Determination of Material Parameters for Microbuckling Analysis of Fiber Reinforced Polymer Matrix Composites," *Int. J. Appl. Mech. Eng.*, vol. 20, no. 2, pp. 373–383, 2015, doi: 10.1515/ijame-2015-0024.

[51] D. Samborsky, J. Mandell, and P. Agastra, "3-D Static Elastic Constants and Strength Properties of a Glass/Epoxy Unidirectional Laminate," *Bozeman Mont. State Univ.*, 2012.

[52] N. Johnson *et al.*, "Investigation of Innovative Rotor Concepts for the Big Adaptive Rotor Project Investigation of Innovative Rotor Concepts for the Big Adaptive Rotor Project," no. September, pp. 1–73, 2019.

APPENDIX A

APPENDIX A: Periodic Boundary Condition Python Function

```python
1  #Adapted from: J.T.B. Overvelde URL: http://www.overvelde.com
2  #Date Retrieved: 11/07/2019
3
4  #FUNCTION TO APPLY PERIODIC BOUNDARY CONDITIONS IN 3D TO THE LATERAL FACES OF A NONLINEAR FIBER KINKING RUC
5  #mdb: model database
6  #NameModel:
7  #NameSet:       A string with the name of your model
8  #Model1dim:     A string with the name of your nodal set that contains all the nodes that will have PBCs applied to them
9  #               An array with the the overall dimensional vectors of the model,
10 #               for example [(1.0,0.0,0.0),(0.0,1.0,0.0),(0.0,0.0,1.0)] for a cubic RUC or RVE
11 #x0y0,x0y1,x1y1,x1y0: Four strings that denote the four nodal sets of the corner nodes that
12 #                     each belong to two sides where PBCs are being applied.
13 def PeriodicBound3D(mdb,NameModel,NameSet,Model1dim, x0y0,x0y1,x1y1,x1y0):
14     import time
15     start1 = time.time()
16
17     from part import THREE_D, DEFORMABLE_BODY
18
19     #Create reference parts and assemble
20     #These will act as the master nodes that will be used to apply macroscopic strains
21     NameRef1= 'RefPoint-0'; NameRef2= 'RefPoint-1';
22     mdb.models[NameModel].Part(dimensionality=THREE_D, name=NameRef1, type=
23         DEFORMABLE_BODY)
24     mdb.models[NameModel].parts[NameRef1].ReferencePoint(point=(0.01, 0.0, 0.0))
25     mdb.models[NameModel].Part(dimensionality=THREE_D, name=NameRef2, type=
26         DEFORMABLE_BODY)
27     mdb.models[NameModel].parts[NameRef2].ReferencePoint(point=(0.0, 0.0, 0.0))
28
29     mdb.models[NameModel].rootAssembly.Instance(dependent=ON, name=NameRef1,
30         part=mdb.models[NameModel].parts[NameRef1])
31     mdb.models[NameModel].rootAssembly.Instance(dependent=ON, name=NameRef2,
32         part=mdb.models[NameModel].parts[NameRef2])
33
34     #Create set of reference points
35     mdb.models[NameModel].rootAssembly.Set(name=NameRef1, referencePoints=(
36         mdb.models[NameModel].rootAssembly.instances[NameRef1].referencePoints[1],))
37     mdb.models[NameModel].rootAssembly.Set(name=NameRef2, referencePoints=(
38         mdb.models[NameModel].rootAssembly.instances[NameRef2].referencePoints[1],))
39
40     end1 = time.time()
41     print end1 - start1
42     start2 = time.time()
```

```python
#Get All edge nodes
nodesx0y0=mdb.models[NameModel].rootAssembly.sets[x0y0].nodes
nodesx0y1=mdb.models[NameModel].rootAssembly.sets[x0y1].nodes
nodesx1y1=mdb.models[NameModel].rootAssembly.sets[x1y1].nodes
nodesx1y0=mdb.models[NameModel].rootAssembly.sets[x1y0].nodes

#Preallocate array for nodal coordinates of corner nodes
nodesx0y0Coor=[]
nodesx0y1Coor=[]
nodesx1y1Coor=[]
nodesx1y0Coor=[]

#Extract nodal coordinates through a for loop for corner nodes in nodesets x0y0, x0y1, x1y1, x1y0
for nodx0y0 in mdb.models[NameModel].rootAssembly.sets[x0y0].nodes:
    nodesx0y0Coor.append(nodx0y0.coordinates)
for nodx0y1 in mdb.models[NameModel].rootAssembly.sets[x0y1].nodes:
    nodesx0y1Coor.append(nodx0y1.coordinates)
for nodx1y1 in mdb.models[NameModel].rootAssembly.sets[x1y1].nodes:
    nodesx1y1Coor.append(nodx1y1.coordinates)
for nodx1y0 in mdb.models[NameModel].rootAssembly.sets[x1y0].nodes:
    nodesx1y0Coor.append(nodx1y0.coordinates)

#Get all side nodes
nodesAll=mdb.models[NameModel].rootAssembly.sets[NameSet].nodes

#Preallocate array for nodal coordinates of all side nodes
nodesAllCoor=[]

#Extract nodal coordinates through a for loop for all nodes in nodeset NameSet
for nod in mdb.models[NameModel].rootAssembly.sets[NameSet].nodes:
    nodesAllCoor.append(nod.coordinates)

end2 = time.time()
print end2 - start2
start3 = time.time()
repConst=0

#Find periodically located nodes and apply equation constraints
ranNodes=range(0,len(nodesAll)) #Index array of nodes not used in equations constraint
print len(nodesAll)
```

```python
83  for repnod1 in range(0,len(nodesAll)):
84      stop=False                          #Stop will become true when equation constraint is made between nodes
85      Coor1=nodesAllCoor[repnod1]         #Coordinates of Node 1
86      for repnod2 in ranNodes:            #Loop over all available nodes
87          Coor2=nodesAllCoor[repnod2]     #Coordinates of Node 2
88          for comb in range(0,len(Model1dim)-1):          #Check if nodes are located exactly the model dimensions apart
89              if int(10000.0*(Model1dim[comb][0]-Coor2[0]+Coor1[0]))==0 \
90              and int(10000.0*(Model1dim[comb][1]-Coor2[1]+Coor1[1]))==0 \
91              and int(10000.0*(Model1dim[comb][2]-Coor2[2]+Coor1[2]))==0:
92                  mdb.models[NameModel].rootAssembly.Set(name='Node-1-'+str(repConst), nodes=
93                  mdb.models[NameModel].rootAssembly.sets[NameSet].nodes[repnod1:repnod1+1])
94                  mdb.models[NameModel].rootAssembly.Set(name='Node-2-'+str(repConst), nodes=
95                  mdb.models[NameModel].rootAssembly.sets[NameSet].nodes[repnod2:repnod2+1])
96                  #Create equations constraints for each dof
97                  for Dim1 in [1,2,3]:
98                      mdb.models[NameModel].Equation(name='PerConst'+str(Dim1)+'-'+str(repConst),
99                      terms=((1.0, 'Node-1-'+str(repConst), Dim1),(-1.0, 'Node-2-'+str(repConst), Dim1) ,
100                     (1.0, 'RefPoint-'+str(comb), Dim1)))
101                 repConst=repConst+1     #Increase integer for naming equation constraint
102                 ranNodes.remove(repnod1)    #Remove used node from available list
103                 stop=True
104                 break                   #Don't look further, go to following node.
105         if stop:
106             break
107
108 repConst1=0
109
110 #Find periodically located edge nodes and apply equation constraints
111 rangeNodesx0y0 = range(0,len(nodesx0y0))    #Index array of corner nodes not used in equations constraints
112 rangeNodesx0y1 = range(0,len(nodesx0y1))    #Index array of corner nodes not used in equations constraints
113 rangeNodesx1y1 = range(0,len(nodesx1y1))    #Index array of corner nodes not used in equations constraints
114 rangeNodesx1y0 = range(0,len(nodesx1y0))    #Index array of corner nodes not used in equations constraints
115 for repnodx0y0 in rangeNodesx0y0:
116     stop=False
117     Coorx0y0=nodesx0y0Coor[repnodx0y0]      #Coordinates of Node in bottom left corner
118     for repnodx0y1 in rangeNodesx0y1:
119         Coorx0y1=nodesx0y1Coor[repnodx0y1]  #Coordinates of Node in top left corner
120         if int(1000.0*(Coorx0y0[2] - Coorx0y1[2])) == 0:    #Check to make sure z coordinate is same between two nodes
121             for repnodx1y1 in rangeNodesx1y1:
122                 Coorx1y1=nodesx1y1Coor[repnodx1y1]          #Coordinates of Node in top right corner
123                 if int(1000.0*(Coorx0y1[2] - Coorx1y1[2])) == 0:    #Check to make sure z coordinate is same between two nodes
```

```python
for repnodx1y0 in rangeNodesx1y0:
    Coorx1y0=nodesx1y0Coor[repnodx1y0]    #Coordinates of Node in bottom right corner
    if int(1000*(Coorx0y0[2] - Coorx1y0[2])) == 0:
        #Create 4 sets in equation constraints
        mdb.models[NameModel].rootAssembly.Set(name='Nodex0y0-'+str(repConst1), nodes=
            mdb.models[NameModel].rootAssembly.sets[x0y0].nodes[repnodx0y0:repnodx0y0+1])

        mdb.models[NameModel].rootAssembly.Set(name='Nodex0y1-'+str(repConst1), nodes=
            mdb.models[NameModel].rootAssembly.sets[x0y1].nodes[repnodx0y1:repnodx0y1+1])

        mdb.models[NameModel].rootAssembly.Set(name='Nodex1y1-'+str(repConst1), nodes=
            mdb.models[NameModel].rootAssembly.sets[x1y1].nodes[repnodx1y1:repnodx1y1+1])

        mdb.models[NameModel].rootAssembly.Set(name='Nodex1y0-'+str(repConst1), nodes=
            mdb.models[NameModel].rootAssembly.sets[x1y0].nodes[repnodx1y0:repnodx1y0+1])

        #Create equation constraint for each DOF
        for Dim1 in [1,2,3]:
            #x0y1 - x1y1 = -MNx
            mdb.models[NameModel].Equation(name='PerConst-top'+str(Dim1)+'-'+str(repConst1),
                terms=((1.0,'Nodex0y1-'+str(repConst1), Dim1),(-1.0, 'Nodex1y1-'+str(repConst1), Dim1),
                (1.0, 'RefPoint-0', Dim1)))

            #x1y1 - x1y0 = MNy
            mdb.models[NameModel].Equation(name='PerConst-right'+str(Dim1)+'-'+str(repConst1),
                terms=((1.0,'Nodex1y1-'+str(repConst1), Dim1),(-1.0, 'Nodex1y0-'+str(repConst1), Dim1),
                (-1.0, 'RefPoint-1', Dim1)))

            #x1y0 - x0y0 = MNx
            mdb.models[NameModel].Equation(name='PerConst-bottom'+str(Dim1)+'-'+str(repConst1),
                terms=((1.0,'Nodex1y0-'+str(repConst1), Dim1),(-1.0, 'Nodex0y0-'+str(repConst1), Dim1),
                (-1.0, 'RefPoint-0', Dim1)))

            repConst1 = repConst1+1
        stop = True #Don't look further, go to following node.
        break
    if stop:
        break
```

```python
end3 = time.time()
print end3 - start3

#Return coordinates of free node so that it can be fixed
return (nodesAll[ranNodes[0]].coordinates, NameRef1, NameRef2)
```